# THESIS FOR THE DEGREE OF DOCTOR OF PHILOSOPHY IN MATERIALS SCIENCE

# Powder Bed Fusion – Laser Beam of a non-weldable Ni-base superalloy ${\rm CM247LC}$

Microstructure control, crack mitigation, heat treatment and creep performance

AHMED FARDAN JABIR HUSSAIN

Department of Industrial and Materials Science
CHALMERS UNIVERSITY OF TECHNOLOGY
Gothenburg, Sweden 2025

## Powder Bed Fusion – Laser Beam of a non-weldable Ni-base superalloy CM247LC

Microstructure control, crack mitigation, heat treatment and creep performance

### AHMED FARDAN JABIR HUSSAIN

ISBN: 978-91-8103-324-3

Acknowledgements, dedications, and similar personal statements in this thesis reflect the author's own views.

## © AHMED FARDAN JABIR HUSSAIN, 2025

Doktorsavhandlingar vid Chalmers tekniska högskola Ny series nr 5781 ISSN 0346-718X https://doi.org/10.63959/chalmers.dt/5781

Department of Industrial and Materials Science Chalmers University of Technology SE-412 96 Gothenburg Sweden Telephone +46 (0)31 772 1000

Cover: Site-specific microstructure tailoring represented by EBSD orientation map in IPF representation. The text  $CAM^2$  is processed with standard stripe width, and the remainder of the sample is processed with short stripe width.

Chalmers Digitaltryck Gothenburg, Sweden 2025

## Powder Bed Fusion – Laser Beam of a non-weldable Ni-base superalloy CM247LC

Microstructure control, crack mitigation, heat treatment and creep performance

#### AHMED FARDAN JABIR HUSSAIN

Department of Industrial and Materials Science Chalmers University of Technology

#### Abstract

Powder Bed Fusion – Laser Beam (PBF–LB) of Ni-base superalloys is highly attractive for components in high temperatures applications, particularly within the aerospace and industrial gas turbine sectors. This interest is due to the high degree of design freedom which allows complex internal cooling channels that significantly improve the component lifetime or enable higher operating temperatures, thereby boosting gas turbine efficiency. However, superalloys containing high volume fraction of  $\gamma'$ , like CM247LC with 60 to 70 vol., exhibit poor PBF-LB processibility, suffering from both micro- and macro-cracking, and have poor and anisotropic creep performance. The aim of the thesis is to understand the impact of the intricate relationships between process parameters, cracking, residual stresses,  $_{
m heat}$ microstructure and creep performance. Using operando synchrotron X-ray radiography, the observed micro-cracking is confirmed to occur during solidification. The microcracks are observed at the high angle grain boundaries exhibiting a distinct solidification structure consistent with the solidification cracking mechanism. Solidification cracking is mitigated either through alloy/powder modification or through process parameter optimization with any remnant solidification cracks eliminated through hot isostatic pressing (HIP). However, the presence of macrocracks, particularly around stress concentrators, is observed after HIP. This macrocracking is identified as strain age cracking (SAC) due to the  $\gamma'$  precipitation. SAC is minimized by a tailored HIP using higher pressure before reaching solution treatment temperature. Minimizing residual stress by varying PBF-LB process parameters, including scan strategies, is effective in minimizing SAC. The solution heat treatment developed for cast CM247LC when applied to CM247LC produced via PBF-LB indicated limited grain growth and poor creep performance. A re-designed HIP combined with a solution heat treatment at higher temperature of 1280 °C demonstrates 23% increase in creep rupture life compared to the standard 1250 °C, yielding slightly coarser grains, improved grain boundary decoration, and finer uniform cuboidal  $\gamma'$  precipitates. Despite this optimization, the creep performance remained inferior to that of the cast alloy. Subsequent tailoring of the PBF-LB process to produce a highly columnar and anisotropic microstructure significantly increased the creep life along the build direction. In summary, this investigation into the PBF-LB of CM247LC demonstrates that the effective mitigation of cracking and improvement of creep performance requires tailored PBF-LB processing and post-processing heat treatment strategies.

**Keywords**: Ni-base superalloy, non-weldable superalloy, powder bed fusion – laser beam, scan strategy, residual stresses, strain age cracking, solidification cracking.

iv	

"Excellence is a continuous process
and not an accident'
Dr. A.P.J. Abdul Kalam
Aerospace Scientist and Former President of India
(1931 - 2015)

## **Preface**

The work presented in this doctoral thesis was conducted at the Department of Industrial and Materials Science at Chalmers University of Technology between December 2021 and December 2025. The work has been carried out under the supervision of Professor Eduard Hryha and Adjunct Professor Håkan Brodin (Siemens Energy AB) with Professor Lars Nyborg acting as the examiner. This work was conducted within the framework of the Centre for Additive Manufacture-Metal (CAM<sup>2</sup>), and the projects Materials for green hydrogen fueled gas turbines through additive manufacturing (MAGDA) and Tailored microstructure control by Additive Manufacturing as enabler for green hydrogen fueled gas turbines (TILDA), both supported by the Sweden's Innovation Agency (VINNOVA).

## List of appended papers:

- Paper I Unveiling crack mitigation pathways in powder bed fusion laser beam of CM247LC: An operando X-ray radiography study of Hf and nano- $Y_2O_3$  additions
  - A. Fardan, G. Soundarapandiyan, V. Pandiyan, S.V. Petegem, E. Polatidis, S. Kazi, S. Goel, C. Pauzon, F. Marone, B. Mehta, A. Parrilli, H. Brodin, E. Hryha
    Manuscript
- Paper II Fine-Tuning Melt pools and Microstructures: Taming Cracks in Powder Bed Fusion – Laser Beam of a nonweldable Ni-base Superalloy

<u>A. Fardan</u>, A. Fazi, R. Peng, T. Mishurova, M. Thuvander, G. Bruno, H. Brodin, E. Hryha
Materialia, 34 (2024), 102059
<a href="https://doi.org/10.1016/j.mtla.2024.102059">https://doi.org/10.1016/j.mtla.2024.102059</a>

- Paper III Microstructure tailoring for crack mitigation in CM247LC manufactured by powder bed fusion laser beam

  A. Fardan, A. Fazi, J. Schröder, T. Mishurova, T. Deckers, G.

  Bruno, M. Thuvander, A. Markström, H. Brodin, E. Hryha

  Additive Manufacturing, 99 (2025), 104672

  https://doi.org/10.1016/j.addma.2025.104672
- Paper IV Role of scan strategies in modulating solidification and strain age cracking in CM247LC processed by powder bed fusion laser beam

  <u>A. Fardan</u>, J. Schröder, J. Xu, H. Brodin, E. Hryha

  Manuscript

Paper V Interplay between  $\gamma'$  precipitation, residual stress and strain age cracking in a high  $\gamma'$  strengthened Ni-base superalloy produced by powder bed fusion – laser beam <u>A. Fardan</u>, T. Mishurova, S. Jakob, G.A. Faria, J. Schröder, A. Evans, M. Thuvander, H. Brodin, E. Hryha Manuscript

Paper VI Overcoming strain age cracking in an additively manufactured non-weldable Ni-base superalloy through HIP

A. Fardan, J. Gårdstam, H. Brodin, E. Hryha Conference proceedings of EuroPM 2024, Sweden https://doi.org/10.59499/EP246281533

Paper VII Impact of hot isostatic pressing on microstructure evolution and creep performance of Powder Bed Fusion – Laser Beam processed CM247LC

A. Fardan, J. Gårdstam, E. Oscarsson, H. Brodin, E. Hryha Advanced Engineering Materials, (2025), 2500691

https://doi.org/10.1002/adem.202500691

Paper VIII On the anisotropic creep behavior of a Ni-base superalloy CM247LC manufactured by powder bed fusion – laser beam

A. Fardan, J. Xu, A. Shaafi Shaikh, J. Gårdstam, U. Klement, J. Moverare, H. Brodin, E. Hryha
Manuscript

## Contribution to appended papers

This section provides a brief description of my contribution to the appended papers. Overall, I planned the experiments in consultation with my supervisors and co-authors. I performed most of the experiments and analysis of results were performed in collaboration with the co-authors. I wrote the first version of each paper in collaboration with my supervisors. The co-authors revised the papers, and I finalized them.

The following indicates what I did not do:

- In Paper I, X-ray radiograph and acoustic emission analysis was performed by Dr. Gowtham Soundarapandiyan at Paul Scherrer Institute/Chalmers and Dr. Vigneashwara Pandiyan at EMPA (Switzerland), respectively.
- In Paper I, the Thermo-Calc simulation was performed by Dr. Bharat Mehta from Thermo-Calc Software AB (Sweden).
- Atom probe tomography (in Paper II, Paper III and Paper V) was performed by Dr. Andrea Fazi and Dr. Severin Jakob at the Division of Microstructure Physics at Chalmers University of Technology supervised by Professor Mattias Thuvander.
- X-ray Computed tomography in Paper II was performed by Dr. Tatiana Mishurova at Bundesanstalt für Materialforschung und-prüfung (BAM) in Berlin (Germany).
- Residual stress measurements and analysis in Paper II were performed by Professor Ru Peng at the Division of Engineering Materials in Linköping University (Sweden).
- Residual stress measurements and analysis in Paper III and Paper IV were performed by Dr. Jakob Schröder and Dr. Tatiana Mishurova at Bundesanstalt für Materialforschung und-prüfung (BAM) in Berlin (Germany).
- Tensile test in Paper IV was done by Dr. Jinghao Xu at the Division of Engineering Materials in Linköping University (Sweden).
- Hot isostatic pressing in Paper IV and Paper VI Paper VIII was performed by Johannes Gårdstam at Quintus Technologies AB in Västerås (Sweden).
- Creep tests in Paper VII were performed by Eva Oscarsson at Siemens Energy AB in Finspång (Sweden).
- The samples in Paper VIII were manufactured by Dr. A. Shaafi Shaikh at EOS Oy in Turku (Finland).
- Creep tests and part of electron microscopy in Paper VIII were done by Dr. Jinghao Xu at the Division of Engineering Materials in Linköping University (Sweden).

## Other papers not appended to the thesis

Paper A Effect of Part Thickness and Build Angle on the Microstructure, Surface Roughness, and Mechanical Properties of Additively Manufactured IN-939

A. Fardan, U. Klement, H. Brodin, E. Hryha

A. Fardan, U. Klement, H. Brodin, E. Hryha Metallurgical and Material Transactions A, Vol 54, 2023, https://doi.org/10.1007/s11661-022-06940-7

Paper B Mapping the mechanical properties of cobalt-based stellite alloys manufactured via blending

R. Ahmed, <u>A. Fardan</u>, S. Davies Advances in Materials and Processing Technologies, <u>https://doi.org/10.1080/2374068X.2023.2220242</u>

Paper C  $\,$  Impact of processing gas composition on process stability and properties of PBF-LB/M processed alloy 718

T. Deckers, <u>A. Fardan</u>, L. Kersting, A. Kreutzer, P. Forêt, S. Dubiez, G. Wit, S. Kleszczynski, U. Klement, H. Brodin Journal of Manufacturing Process, <a href="https://doi.org/10.1016/j.jmapro.2024.04.061">https://doi.org/10.1016/j.jmapro.2024.04.061</a>

Paper D A novel alloy design approach in developing CoNi-based high entropy superalloy using high entropy alloys thermodynamic and spark plasma sintering

A. Mohammadzdeh, A. De Nardi, F. Omidbakhsh, D. Garbiec, <u>A. Fardan</u>, E. Hryha, A. Mostafaei, J. M. Torralba Materials Science and Engineering: A <a href="https://doi.org/10.1016/j.msea.2024.146841">https://doi.org/10.1016/j.msea.2024.146841</a>

## Table of contents

1.	$\operatorname{Intr}$	oduction 1	_
	1.1.	Background 1	L <b>-</b>
	1.2.	Problem description 2	2 -
	1.3.	Research questions 2	2 -
2.	Ni-b	pase superalloys	} -
	2.1.	History and development of Ni-base superalloys 3	} -
	2.2.	Microstructure and phases	Į -
	2.3.	Alloy CM247LC 6	<b>;</b> -
3.	Pow	vder Bed Fusion – Laser Beam (PBF–LB) 7	7 –
	3.1.	PBF-LB principle 7	7 –
	3.2.	PBF-LB process parameters 8	3 -
	3.3.	Defects in PBF–LB processed parts 10	) –
	3.4.	Microstructure of PBF–LB processed parts in as-built condition 12	2 -
	3.5.	Residual stress 13	} -
	3.6.	Post-process heat treatment 13	} -
4.	Cha	dlenges in PBF–LB of Ni-base superalloys 15	<u> </u>
	4.1.	Micro-cracking 15	<u> </u>
	4.2.	Macro-cracking 16	<b>;</b> -
	4.3.	Microstructure and mechanical performance 17	7 –
5.	Met	hodology 19	) -
	5.1.	Material 19	) -
	5.2.	PBF-LB process 19	) -
	5.3.	Heat treatment 20	) –
	5.4.	Metallographic preparation 20	) -
	5.5.	Optical Microscopy 21	L <b>-</b>
	5.6.	Scanning Electron Microscopy 21	L <b>-</b>
	5.6.	1. SEM imaging and chemical analysis 22	2 -
	5.6.5	2. Electron backscattered diffraction 22	2 -
	5.6.3	3. Electron channeling contrast imaging 22	2 -
	5.7.	Atom probe tomography 23	} -
	5.8.	X-ray diffraction 23	} -
	5.9.	Creep testing 24	1 -

6.	Summar	ry of results 25 -
6	6.1. Mic	cro-cracking 25 -
	6.1.1.	Micro-cracking mechanism 25 -
	6.1.2.	Micro-cracking mitigation 25 -
(	6.2. Mac	cro-cracking 27 -
	6.2.1.	Macro-cracking mechanism 27 -
	6.2.1.	Macro-cracking mitigation 27 -
	6.2.2.	Macro-cracking mitigation by heat treatment 29 -
(	6.3. Cre	ep performance 30 -
	6.3.1.	Impact of PBF–LB process 30 -
	6.3.2.	Impact of heat treatment 31 -
7.	Conclus	ions 33 -
8.	Future v	work 35 -
Ac	knowledge	ements 37 -
Ro	ferences	_ 30 _

## List of abbreviations

AM Additive manufacturing APT Atom probe tomography

BD Build direction

BSE Backscattered electron CAD Computer aided design

cECCI Controlled electron channeling contrast imaging

DDC Ductility dip cracking
DEC Diffraction elastic constant
DS Directional solidification

EBSD Electron backscattered diffraction ECCI Electron channeling contrast imaging

EDM Electrical discharge machining EDS Energy dispersive spectroscopy

FCC Face-centered cubic GA Gas atomization

HAGBs High angle grain boundaries

HIP Hot isostatic pressing
IPF Inverse pole figure
LED Linear energy density
LMP Larsson-Miller Parameter

LoF Lack of fusion
OM Optical microscopy
PBF Powder bed fusion

PBF-LB Powder bed fusion – laser beam

PX Polycrystalline
RQ Research question
RS Residual stress
SAC Strain age cracking

S-XRD Synchrotron X-ray diffraction

SE Secondary electron

SEM Scanning electron microscope SOM Stereo optical microscope

SX Single crystalline

TCP Topologically close packedVED Volumetric energy densityVIGA Vacuum inert gas atomization

XRD X-ray diffraction

## 1. Introduction

## 1.1. Background

Powder Bed Fusion – Laser Beam (PBF–LB) of metals is a prominent metal additive manufacturing (AM) technology belonging to the category of powder bed fusion (PBF) [1]. Its principal advantage is the freedom of design it offers, enabling the fabrication of highly complex geometries often unattainable by conventional manufacturing routes. In contrast, subtractive and forming processes, which still dominate the manufacturing chain, are restricted by tooling constraints and geometrical limitations. Moreover, the layer-by-layer nature of PBF–LB improves material efficiency by reducing waste and facilitates rapid design iterations, making the technology highly attractive for high-performance applications. The maturity of PBF–LB is reflected in its increasing adoption across aerospace, energy, and biomedical sectors [2].

Despite these technical advantages, PBF–LB remains more expensive than many conventional manufacturing routes. Consequently, its economic feasibility is therefore strongest for complex, small-to-medium batch components, where conventional processes are either equally costly or technically unfeasible. In the aerospace and energy sectors, PBF–LB has already been applied to critical hot gas path components such as turbine vanes and blades [3,4]. Specifically, the ability to integrate intricate internal cooling channels into turbine blades, for example, provides several benefits, including extended component lifetime, reduced cooling air consumption, and allows for higher operating temperatures, all of which fundamentally enhance overall turbine efficiency [5].

However, the widespread application of PBF–LB is severely constrained by the limited processability of certain alloys, particularly  $\gamma'$ -strengthened Ni-base superalloys that are typically used for hot gas path components in turbines. These alloys, typically produced by investment casting, are valued for their exceptional creep resistance and oxidation resistance at elevated temperatures [6]. A prominent example is CM247LC, developed by Cannon-Muskegon Corporation [7], a derivative of MAR-M247 developed by Martin Metals Corporation [8]. CM247LC is a polycrystalline superalloy (equiaxed or directionally solidified) which is widely employed for load-bearing components like blades and vanes in gas turbines for energy production [7]. Its superior high temperature capability comes from its increased Al content, which improves oxidation resistance (by forming protective Al<sub>2</sub>O<sub>3</sub>) and creep resistance (due to a high  $\gamma'$  volume fraction of ~60-70%). Despite being manufactured primarily through casting, there is an increasing interest in manufacturing CM247LC components via AM methods, such as PBF–LB, due to the unique design freedom and repair capabilities they offer.

## 1.2. Problem description

PBF–LB process involves rapid solidification, steep thermal gradients, and cyclic reheating, conditions like those encountered in welding that promote cracking in CM247LC and lead to the alloy being classified as non-weldable. The industrial deployment of CM247LC (and other high  $\gamma'$  volume-fraction superalloys) is significantly restricted by the three identified challenges:

- Micro-cracking: Micron-sized cracks observed after the PBF-LB process.
- Macro-cracking: Larger cracks observed near stress concentrators after postprocessing heat treatment.
- Fine and anisotropic microstructure resulting in poor high temperature mechanical performance, particularly creep resistance.

## 1.3. Research questions

This doctoral thesis investigates the challenges associated with processing of CM247LC via PBF–LB. Specifically the research focuses on understanding and mitigating various cracking phenomena that limit its processability, followed by tailoring PBF–LB processing and post-processing heat treatment to achieve optimal microstructure and creep performance. The thesis addresses the following research questions (RQs):

**RQ1**: What is the mechanism of micro-cracking during PBF–LB processing of CM247LC, and how can it be mitigated?

**RQ2**: What is the mechanism of macro-cracking during post-processing heat treatment of PBF–LB processed CM247LC, and which factors influence it?

**RQ3**: How does PBF–LB processing and heat treatment affect the microstructure and creep performance of CM247LC?

The RQs are addressed in the appended papers as indicated by the Table below.

	RQ1	RQ2	RQ3
Paper I			
Paper II			
Paper III			
Paper IV			
Paper V			
Paper VI			
Paper VII			
Paper VIII			

## 2.1. History and development of Ni-base superalloys

Ni-base superalloys are an important class of materials developed for use at elevated temperatures due to their superior strength, corrosion and/or oxidation resistance [9]. Because of these excellent properties, they are often used in demanding applications, such as the hot sections of gas turbines for civil aircraft or power generation [10]. The efficiency of a gas turbine is directly related to the temperature of the hot gases entering it; therefore, increasing this temperature improves efficiency. However, this places a heavy demand on the components, requiring them to sustain high mechanical loads and surface degradation as gas temperatures can approach 1200 to 1500 °C, a range where most alloys, including Ni-base superalloys, cannot operate unaided. Therefore, components in the hot sections of a gas turbine, such as turbine blades, typically rely on a combination of techniques, including internal cooling and thermal barrier coatings, to sustain operation [11].

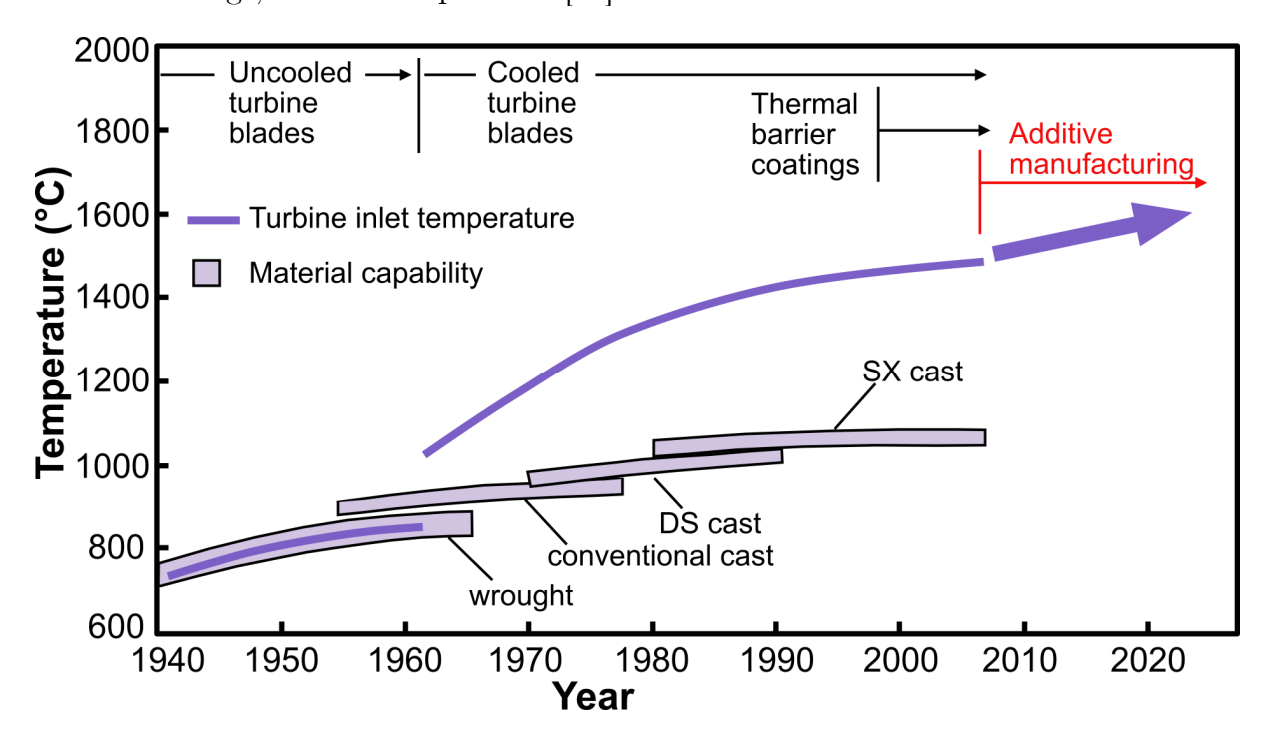


Figure 1. Evolution of turbine inlet temperature in industrial gas turbines. Adapted from [12–15].

The increasing demand for gas turbine operation at high temperatures has driven significant improvement in both the alloys and their manufacturing processes as illustrated in *Figure 1*. As the operating temperature increases, the requirement for mechanical performance, particularly creep resistance, also increases. Creep refers to the time-dependent, inelastic and irrecoverable deformation that occurs for alloys at high temperature due to various thermally activated processes [11]. Historically,

casting has been the preferred method for manufacturing turbine blades because it offers superior creep performance compared to the wrought process. The first major advancement in casting led to microstructural tailoring, transitioning from a polycrystalline equiaxed (PX) structure to a columnar structure using directional solidification (DS) technology. Up until this point, the PX structure consisted of multiple grains and grain boundaries which limited the creep performance. The final critical improvement in casting came with the single crystal (SX) technology, which eliminated all grain boundaries enabling improved creep performance.

These advancements in casting, combined with the use of thermal barrier coatings, have been crucial in achieving higher turbine inlet temperatures and greater engine efficiency. The advancement in additive manufacturing and its design freedom is particularly attractive for the gas turbine industry, especially due to the capabilities of even further improvement in cooling performance within components. Looking ahead, the introduction of hydrogen-fueled gas turbines characterized by even higher temperatures and more aggressive operating conditions will place higher demands on Ni-base superalloy components and drive further innovation in manufacturing technologies. This evolving landscape highlights the critical need for high strength alloys with improved design suited for hydrogen combustion, a challenge potentially solvable by additive manufacturing [13–15].

## 2.2. Microstructure and phases

Ni-base superalloys have complex compositions, often containing ten or more elements, which enable their effective use at elevated temperature. Their microstructure consists primarily of a disordered  $\gamma$  (gamma) matrix along with secondary phases that determine material performance, including the ordered  $\gamma'$  (gamma prime) precipitates, carbides and borides. This section reviews the influence of the alloying elements, the resulting microstructure, and the phases with a particular emphasis on PX  $\gamma'$  strengthened Ni-base superalloys.

The  $\gamma$  matrix consists of a disordered face-centered cubic (FCC) structure. It features a broad solubility for secondary alloying elements, including high melting point refractory elements. The matrix is composed of Ni along with other elements such as Cr, Co, Mo, Ta and W in higher concentrations, all of which contribute to solid solution strengthening [9,16].

The  $\gamma'$  precipitates are the most important strengthening phase in  $\gamma'$  strengthened Nibase superalloys. They possess an ordered FCC (L1<sub>2</sub>) crystal structure comprised mainly of Al in the corner of an FCC lattice with Ni in the face centers. Ti and Ta are also present in the  $\gamma'$  precipitates and aid in increasing the volume fraction of  $\gamma'$  [11]. The  $\gamma'$  precipitates are coherent precipitates, and their morphology depends on the alloy composition and heat treatment. Typically  $\gamma'$  precipitates are cuboidal-shaped and uniformly dispersed throughout the  $\gamma$  matrix, however they can also be found at the grain boundaries as a continuous film [16].

Besides the  $\gamma$  matrix and  $\gamma'$  precipitates, other phases like carbides and borides are present in small amounts and strengthen grain boundaries, thereby improving creep resistance. Firstly, carbides can be subdivided into two types - primary and secondary carbides. Primary carbides are of the MC-type where M refers to metallic element and C to carbon. MC carbides form during the solidification process and are usually found in the inter-dendritic region. They have an FCC crystal structure and lack a preferred orientation relationship with the  $\gamma$  matrix. MC carbides act as a source of carbon for the alloy during heat treatment and service. The 'M' (metallic element) in MC is usually a refractory or reactive element; common examples include HfC, TaC, NbC and TiC. It is common for multiple metallic elements to substitute for one another within the MC carbide [9].

The secondary carbides (M<sub>23</sub>C<sub>6</sub> and M<sub>6</sub>C) form at elevated temperature from the degeneration of MC carbides. M<sub>23</sub>C<sub>6</sub> forms at lower temperature (760 to 980 °C), while M<sub>6</sub>C forms at a slightly higher temperature (815 to 980 °C). Both the secondary carbides are found at the grain boundaries and hinder grain boundary sliding thereby improving creep resistance. Furthermore, due to the higher stability of M<sub>6</sub>C they are beneficial to control grain size during thermomechanical processing. Both secondary carbides are comprised of Cr, Mo and W, however M<sub>6</sub>C is more likely to form when the Mo and W concentrations are higher.

Boron (B) is an important alloying element for PX superalloys and is present to the extent of 50 – 500 ppm. It is considered a grain boundary strengthener that improves creep performance. B reacts with metallic elements to form various types of borides (M<sub>2</sub>B, M<sub>3</sub>B<sub>2</sub>, M<sub>5</sub>B<sub>3</sub>) potentially containing Mo, Cr and W [17–19]. Borides are hard refractory particles with blocky or half-moon appearance, typically located at grain boundaries and act as supply of B to the grain boundary [9].

Zirconium (Zr), like B is another element which improves the creep performance for PX superalloys. Zr limits the agglomeration of M<sub>23</sub>C<sub>6</sub> carbides at grain boundaries and limits the formation of void/crack during creep [16]. Additionally, Zr is also known to be a 'getter' of tramp elements such as sulfur and phosphorous which are melting point depressants [11]. However, the role of Zr in improving creep performance has been questioned in the literature [20].

Topologically close packed (TCP) phases are intermetallic compounds that can form due to long-term exposure to high temperatures during service or heat treatment.

Common TCP phases are  $\sigma$  (sigma),  $\mu$  (mu) or Laves and contain elements such as Cr, Mo and W. They exhibit a plate-like or needle-like morphology and negatively influence creep life and ductility. Consequently, significant effort is dedicated to avoid the compositional ranges where TCP phases can form [9,11].

## 2.3. Alloy CM247LC

CM247LC is a modified Ni-base superalloy [6,7], derived from MAR-M247 [8], and optimized for DS casting. The compositions of both the alloys are shown in Table~1. Notable chemistry modification includes lowering the amount of Ti and Zr, along with tight control of Si and S to eliminate grain boundary cracking. Additionally, the C content was lowered to improve carbide morphology and stability accompanied by good intermediate temperature ductility. Cr, Ti, W and Mo were lowered to minimize the detrimental  $\sigma$  (sigma) TCP phase. CM247LC has excellent high temperature performance (high creep resistance and oxidation resistance) and is therefore used to manufacture turbine blades and vanes in gas turbine engines [6]. The excellent high temperature performance is due to the relatively higher Al content compared to that of other Ni-base superalloys (such as IN718, Haynes 282®, IN939, IN738LC [21]). High Al content enhances creep resistance by increasing the volume fraction and stability of  $\gamma'$  precipitates and improves oxidation resistance by forming a protective Al<sub>2</sub>O<sub>3</sub> scale. Both effects are crucial for reliable performance of turbine components at extreme temperatures.

**Table 1.** Chemical composition (nominal in wt.%) showing selected elements for MAR-M247 and CM247LC [6]

	$\mathbf{Cr}$	Co	Mo	$\mathbf{C}$	$\mathbf{W}$	Hf	Ta	${f Ti}$	Al	$\mathbf{Zr}$	В	Ni
MAR-	8.4	10.0	0.7	0.15	10.0	1.5	3.0	1.0	5.5	0.05	0.015	Bal.
M247												
CM247LC	8.1	9.2	0.5	0.07	9.5	1.4	3.2	0.7	5.6	0.015	0.015	Bal.

The ongoing transition to hydrogen-fueled gas turbines and the pursuit of higher thermal efficiency have increased the demand for higher operating temperatures [13–15]. This shift increases the need for superalloys with exceptional creep and oxidation resistance, making CM247LC a key candidate. Traditionally, CM247LC components have been produced by investment casting. However, achieving the advanced cooling strategies with the increasing demand of operating temperatures now necessitates the adoption of additive manufacturing technologies such as PBF–LB. PBF–LB allows design freedom, enabling the incorporation of complex internal cooling channels, an essential feature for high-performance components such as turbine blades and vanes in gas turbines. Nevertheless, several challenges arise during the PBF–LB processing and post-processing of CM247LC which is further addressed in Section 4.

## 3. Powder Bed Fusion – Laser Beam (PBF–LB)

Conventional manufacturing technologies such as casting, forging, and machining have historically been the core methods used to manufacture metallic components. Casting involves pouring molten metal into a mold; forging relies on plastic deformation; and machining achieves the final shape through the removal of material i.e. subtractive manufacturing. However, these traditional processes often lead to significant material wastage, longer lead times, and limited design freedom.

In contrast, additive manufacturing (AM), commonly known as 3D printing, builds components in a layer-by-layer fashion, offering several advantages over conventional techniques. AM fundamentally unlocks design freedom that was previously unattainable, as conventional designs were often limited in complexity by the restricted capabilities of cutting tools and jigs/fixtures. Furthermore, while the cost of a component typically increases with its complexity in conventional manufacturing methods; AM allows complex geometries, internal cooling channels, and lattice structures to be manufactured easily without a proportional increase in manufacturing costs. This combination of design freedom and the reduced need for dedicated tooling is a main driver for AM adoption across numerous sectors. Additionally, AM's capabilities for on-demand manufacturing with reduced lead times and its inherent repair potential have significantly increased industry interest.

AM technologies are diverse and can be broadly divided into seven categories [22]. Powder Bed Fusion (PBF) is one of these seven, which is capable of consolidating metals and polymers. This process generally involves a powder bed where particles are fused using a thermal source, such as a laser or an electron beam. Specifically, this thesis deals with metal powders consolidated with a laser beam, known as PBF-LB of metals. Details regarding PBF-LB, including its working principle, process parameters, characteristic defects, and microstructure evolution, will be discussed in the following sections.

## 3.1. PBF-LB principle

A typical PBF–LB machine consists of building platform, recoater, powder dispenser, powder collector and the laser system (laser and scanner), indicated in Figure 2. The process starts with a three-dimensional CAD (computer aided design) file which is sliced to two-dimensional slices based on the chosen layer thickness (~20 to 80 μm). These two-dimensional slices are then transferred to the PBF–LB machine with each slice containing the layer information. The powder from the dispenser is deposited on the building platform with the help of a recoater. The laser system then scans and melts the powder based on the layer information. The recoater moves back to the start

position and the build platform then moves down a designated layer thickness while the dispenser moves up. The recoater then deposits the second layer of powder followed by the laser system scanning the next layer of the part to be manufactured. This layerby-layer process proceeds until the desired component is obtained. The metal powder feedstock used for the PBF-LB is typically produced by gas atomization (GA) and have a spherical morphology with powder size in the range of 15 to 63 µm. Ni-base superalloys are typically produced using Vacuum Inert Gas Atomization (VIGA) process due to the presence of oxidation sensitive elements like Al and Ti [23], but are also produced using other atomization methods such as plasma atomization (PA) and Electrode Induction melting Gas Atomization (EIGA) [23]. A micrograph showing the VIGA powder of a typical Ni-base superalloy is shown in the inset of Figure 2. It is to be noted that the entire PBF-LB process takes place inside the build chamber with an inert atmosphere, typically Ar, to reduce the oxidation during the process. Once the build is completed the unmelted powder is removed from the powder bed and can be reused after sieving. The part is separated from the building platform using a bandsaw or by electrical discharge machining (EDM).

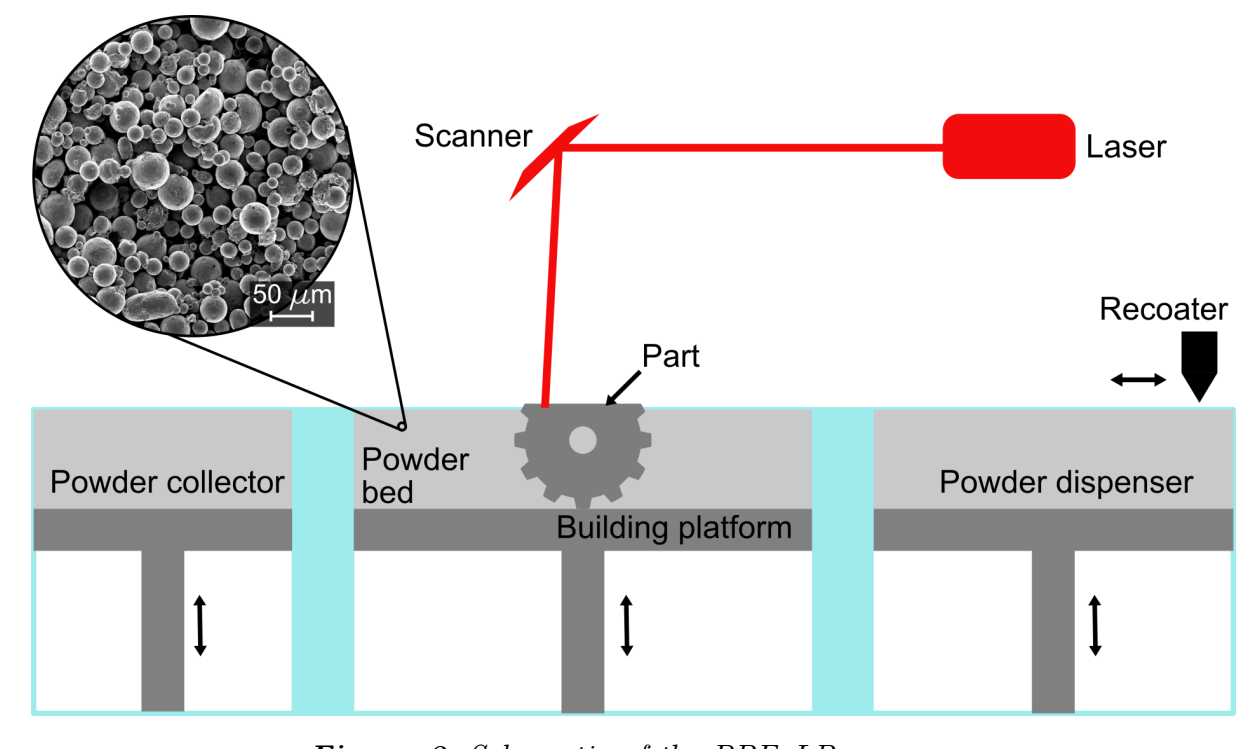


Figure 2. Schematic of the PBF-LB process.

## 3.2. PBF-LB process parameters

The quality of the parts manufactured by PBF–LB process is influenced by the chosen process parameters. Most of the structural applications require high density parts with good mechanical performance that require careful optimization of the process parameters. There are several process parameters that can be varied in PBF–LB.

However, the main parameters that are typically considered for process optimization include laser power (P), laser scan speed (v), hatch distance (h) and layer thickness (t). Figure 3 highlights a schematic of the PBF-LB process where the main process parameters are depicted. As the laser scans over a pre-determined path over the powder bed, it forms a melt pool that melts and solidifies. The laser power (P) and laser scan speed (v) typically determine the shape and size of the melt pool and are represented as linear energy density (LED), as shown in Eqn. (1).

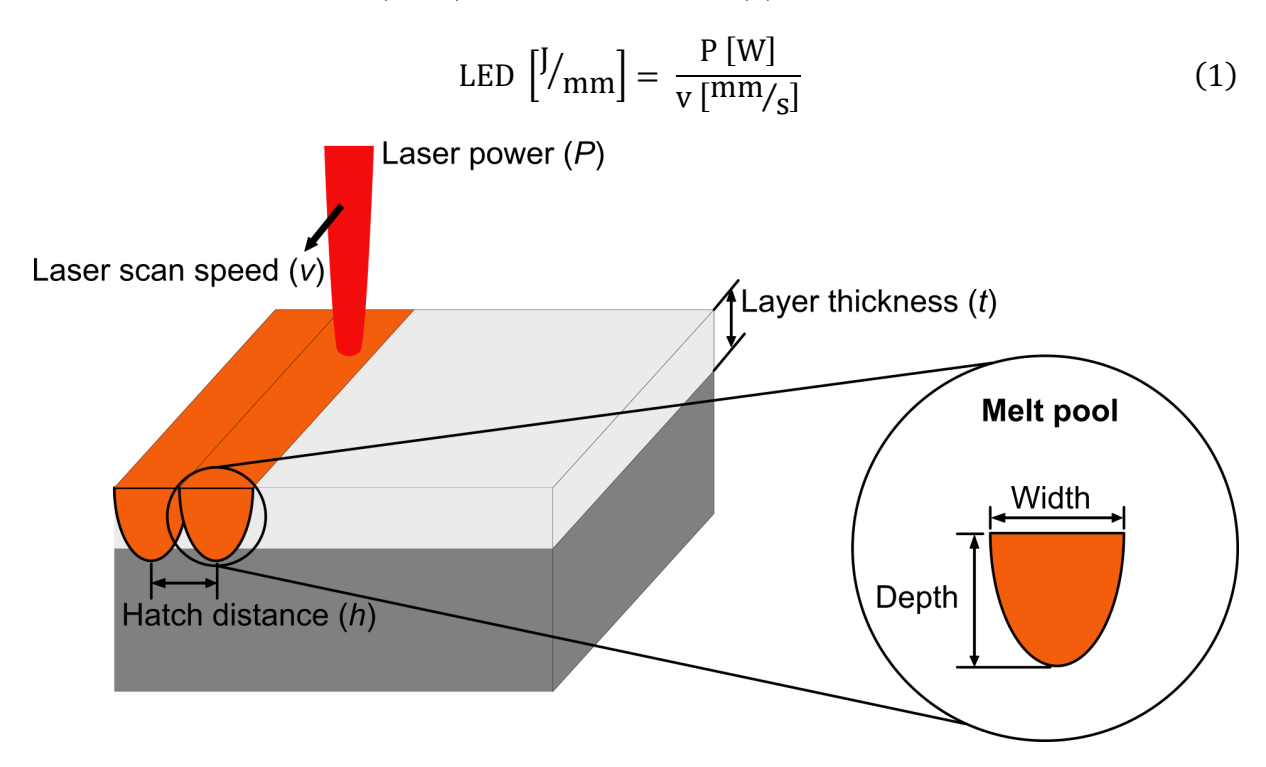


Figure 3. Schematic of the printing process in PBF-LB highlighting the main process parameters along with melt pool dimensions.

Higher LED values lead to deeper and wider melt pools, while lower LED leads to shallower and narrower melt pools. Another important parameter to be considered is hatch spacing, which refers to the spacing between two adjacent melt tracks. It is crucial to have sufficient overlap between the adjacent tracks to avoid the formation of lack of fusion porosity. Finally, layer thickness is another important parameter that determines the volume of powder that needs to be melted. Typical layer thickness values are 20 to 40 µm but larger layer thicknesses up to 80 µm has been explored for some materials to increase productivity [24,25]. A combination of parameters known as volumetric energy density (VED) is used to represent the main process parameters as shown in Eqn. (2).

$$VED \left[ \frac{J}{mm^3} \right] = \frac{P[W]}{v[mm/_S].h[mm].t[mm]}$$
 (2)

Apart from the main parameters mentioned above, scan strategy is another crucial parameter. Scan strategy refers to the path the laser scan follows in a particular and subsequent layers. Figure 4 depicts some of the scan strategies. It is to be noted that a bi-directional stripe scan strategy along with rotation angle of  $67^{\circ}$  (Figure 4d) is commonly used in industrial machines. The chosen process parameters along with the scan strategy can affect defect formation, residual stresses, microstructure and in turn the mechanical performance [26–28].

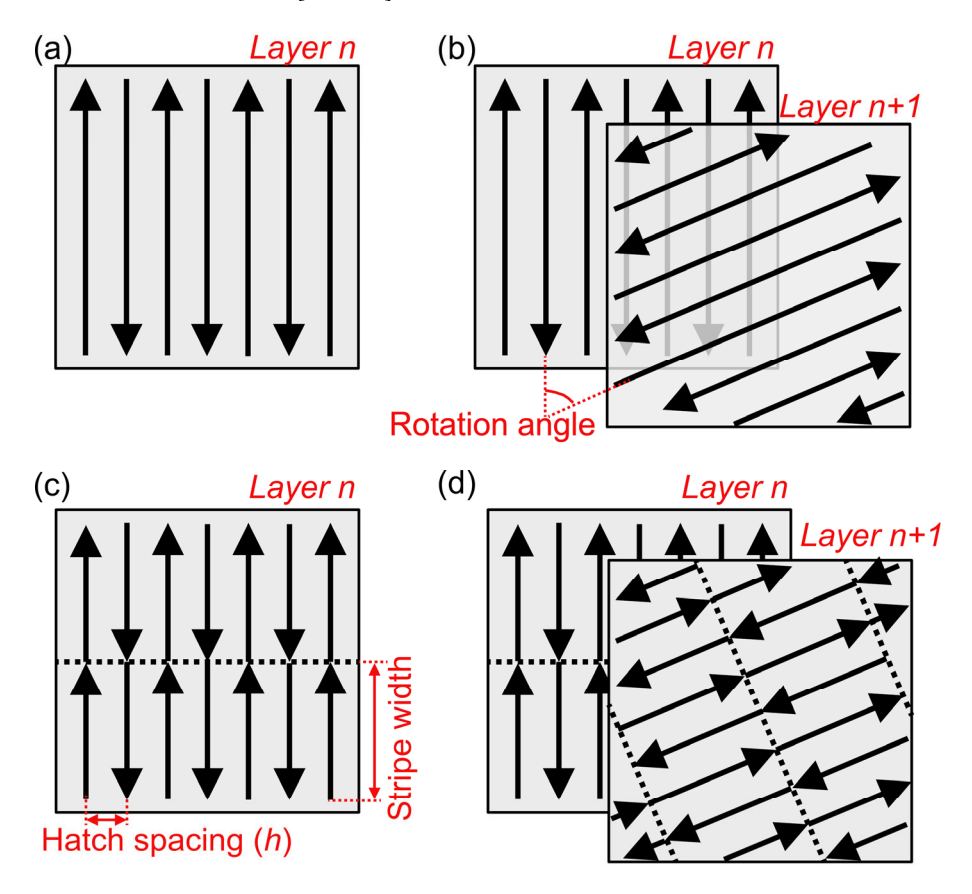


Figure 4. Schematic of selected scan strategies in PBF-LB (a) bi-directional scan strategy, (b) bidirectional scan strategy with rotation, (c) stripe scan strategy, (d) stripe scan strategy with rotation.

## 3.3. Defects in PBF-LB processed parts

Different types of porosity can be found in samples manufactured using the PBF–LB process. Some of the commonly process-induced porosities include lack of fusion and keyhole.

Keyhole porosity (*Figure 5a*) refers to the porosity that is caused by the high energy input to the material, which leads to material vaporization and creation of nearly spherical pores, typically found in the bottom of the melt pool. This type of porosity can be mitigated by lowering the energy input or post-processing HIP.

Lack of fusion (LoF) porosity (Figure 5b) refers to the porosity that is caused by the improper melting of the powders and can be found either between adjacent melt tracks or between layers. This is often caused by either improper horizontal overlaps between melt tracks or improper vertical overlap between layers. LoF porosity tends to have sharp edges and irregular morphology which can be detrimental for cyclic loading such as fatigue. Therefore, it is important for superalloys that are intended to be used in critical applications to avoid LoF porosity. This is achieved either through having sufficient horizontal or vertical overlaps through optimized hatch spacing or increased energy input (VED or LED). Minimizing LoF porosity through HIP is possible, however it is challenging to eliminate due to the presence of trapped Ar gas [29,30].

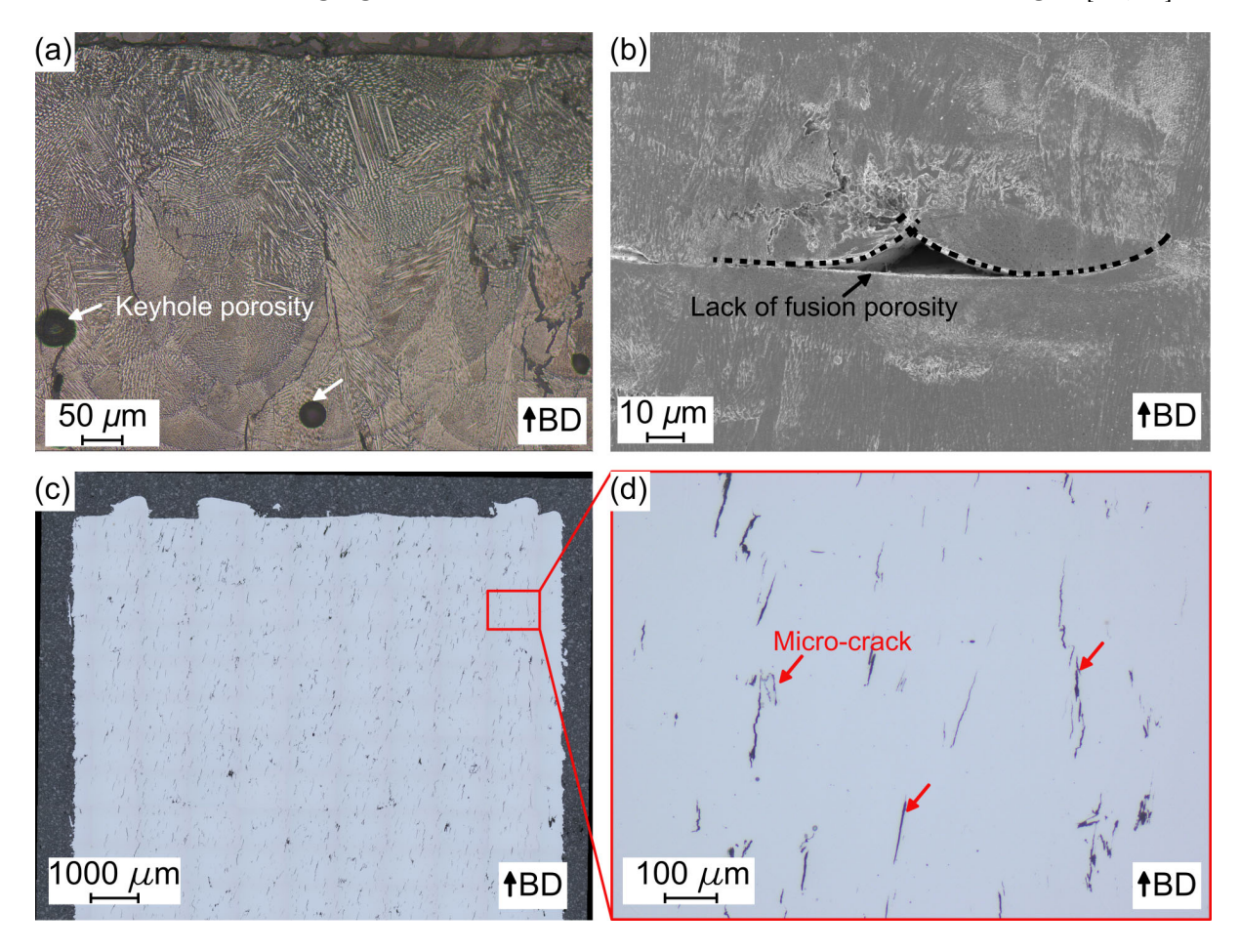


Figure 5. Defects in PBF-LB processed parts. (a) Keyhole porosity, (b) Lack of fusion porosity, (c),(d) Micro-crack. All micrographs are from CM247LC processed by PBF-LB.

It is to be noted that processing window of an alloy typically lies between the lack of fusion and keyhole mode [31]. This processing window sometimes referred to as conduction mode is wide for most of the alloys including some low- $\gamma'$  strengthened superalloys such as Haynes 282® [32]. However, micro-cracking is observed in some medium to high  $\gamma'$  strengthened superalloys (Figure 5c,d) which limits the processing

window [19,33,34]. Further details on micro-cracking mechanism and its mitigation can be found in *Section 4.1*.

3.4. Microstructure of PBF-LB processed parts in as-built condition PBF-LB is a complex process that involves repeated melting and solidification of an alloy along with high cooling rates ( $\sim 10^5$  to  $10^6$  K/s) in PBF-LB process [35,36]. Coupled with the complex thermal history due to re-melting of adjacent tracks and subsequent layers, the process can induce complex phase transformations, crystallographic texture and non-equilibrium microstructures in the as-built condition. This necessitates post-processing heat treatments for  $\gamma'$  strengthened Ni-base superalloys. The current section will review the important microstructural features in  $\gamma'$  strengthened Ni-base superalloys in the as-built PBF-LB condition.

When the laser interacts with the metal powder, a melt pool is formed which then solidifies. The solidification structure is influenced by the temperature gradient (G) and the growth rate (R). It has been established that the combination of high temperature gradient and growth rate leads to a cellular-like solidification structure comprising of primary dendrites. The direction of the primary dendrites is influenced mainly by the shape and size of the melt pool, which, in turn, affects the crystallographic texture. A narrow and shallow melt pool promotes the formation of a strong <100> crystallographic texture along the build direction, while a wide and deep melt pool would have a strong <110> crystallographic texture.

It is to be noted that the primary dendrites solidify first followed by the interdendritic region which leads to a compositional difference between the dendrite core and the interdendritic region. Elements such as Hf, Al, Ta, Ti, B, Zr, Mo, Cr, Co and Nb tend to segregate to the interdendritic region [37–39]. The segregation to the interdendritic regions in Ni-base superalloys leads to the formation of primary carbides (MC carbide) [40,41],  $\gamma/\gamma'$  eutectic [38] and possibly tetragonal close packed (TCP) phases [41].

It is to be noted that the formation of  $\gamma'$  precipitates in as-built microstructure is generally limited or avoided due to the high cooling rates associated with the PBF-LB process [21,40,42]. However, the local chemistry variation, especially in interdendritic region with the presence of higher content of  $\gamma'$  forming elements (Al+Ti) can lead to the formation of  $\gamma'$  precipitates. These  $\gamma'$  precipitates are ~10 to 30 nm in size as identified by transmission electron microscopy (TEM) or atom probe tomography (APT) [43,44]. Some studies have also identified  $\gamma'$  precipitates from synchrotron X-ray diffraction (S-XRD) in CM247LC and IN713LC [45]. However, identification of  $\gamma'$  in as-built condition using lab-based XRD is difficult due to the limited resolution/energy of the X-rays [46].

## 3.5. Residual stress

Residual stresses are self-balanced stresses that remain in a material after manufacturing without any acting external stresses. Residual stresses can be beneficial or detrimental to the performance of a component depending on their nature and magnitude.

Depending on the length scale of the residual stresses, they can be classified into three types: 1) Type-I are residual stresses that occur on component level i.e. macro-scale and is also known as macro residual stress; 2) Type-II are residual stresses that occur on grain or phase level and 3) Type-III are residual stresses that occur at atomic scale such as point defects, vacancies or dislocations. Both Type-II and Type-III collectively are known as micro residual stress [47,48]. In fact, residual stress at a point is a combination of the three types of residual stresses [49].

In PBF–LB, high value of residual stresses present in the component is due to the localized energy input, constrained shrinkage along with the complex thermal history. The high residual stresses often lead to distortion when removing components from the build plate and necessitate stress relief heat treatments for complex components. The residual stresses in as-built PBF–LB components are influenced by the chosen process parameters, scan strategies or size/geometry of the component.

## 3.6. Post-process heat treatment

Several alloys are used in as-built condition due to the superior tensile strength (limited ductility) given by the fine microstructures. However, there could be a necessity for performing stress relief heat treatments for larger parts attached to the build platform to prevent warpage/deformation. Furthermore, solution and ageing heat treatments may be required to homogenize and obtain the required strengthening phases. This is crucial for Ni-base superalloys strengthened by  $\gamma'$  to achieve the intended microstructure and mechanical performance.

Hot isostatic pressing (HIP) is an important post-process heat treatment that is effective in minimizing defects [50] including micro-cracks [51]. HIP involves heating up a component combined with applying high pressures (100 to 200 MPa) with the help of inert gas such as Ar. At high temperature the flow stress of the material decreases along with increased atomic diffusion. When the applied pressure by the gas exceeds the material flow stress, this results in plastic deformation and material flow resulting in closure of defects [30]. Due to this effectiveness of HIP in closing defects, it is an important part of routine heat treatment for critical components (cast turbine blades) made of Ni-base superalloys. Furthermore, HIP can be combined with other heat treatments such as solution and ageing heat treatments [30].

It is to be noted that there is a need for re-development of heat treatment, particularly the first heat (solution) treatment after PBF–LB process, especially for  $\gamma'$  strengthened Ni-base superalloys [52–54].

## 4. Challenges in PBF-LB of Ni-base superalloys

## 4.1. Micro-cracking

A common and significant challenge reported in PBF–LB processing of superalloys is micro-cracking. Both precipitation [55] and solid-solution strengthened [56] superalloys have reported occurrence of micro-cracking. These cracks are small and are typically on length scale of the melt pool. While various mechanisms have been proposed, the majority of reports attribute micro-cracking in PBF–LB processed superalloys primarily to solidification cracking [57–59].

Solidification cracking, sometimes also known as hot tearing or hot cracking, appears during the solidification process. They have been identified earlier in casting [60] and welding [61]. It is generally accepted that this type of cracking occurs due to insufficient liquid feeding into the interdendritic regions during the terminal stages of solidification coupled with thermal stresses and shrinkage during solidification [61]. The presence of liquid film is due to the larger solidification interval that leads to the presence of liquid films in the interdendritic boundaries which makes it susceptible to solidification cracking. Therefore, these cracks tend to have a dendritic appearance on the crack surface and are typically intergranular [62,63].

The attempts to minimize micro-cracking have been achieved either through alloy modifications or process optimization. Alloy modification involved reduction of elements that tend to segregate to interdendritic/grain boundaries such as Hf, B, Zr, Si, etc. [38,64–67]. Although tramp elements such as Si can be minimized, other elements such as Hf, B and Zr are crucial for high temperature creep performance [68,69]. Additionally, incorporating nanoparticles such as TiC [70] have shown to cause wider and shallower melt pools along with grain refinement which subsequently minimizes micro-cracking. Moreover, certain nanoparticles like Y<sub>2</sub>O<sub>3</sub> [71] can interact with the base alloy and trap elements like Zr prone to segregation that effectively minimizes solidification cracking.

Process optimization involving laser parameters (laser power and speed), hatch spacing and scan strategy have been demonstrated to influence micro-cracking. One of the earliest works [72] on CM247LC produced by PBF-LB indicated that micro-cracking is minimized by using lower linear energy density (LED given by Eqn. (1)). However, this increased the risk of lack of fusion that can be circumvented by reducing the hatch spacing. The effectiveness of lower LED in minimizing micro-cracking was also confirmed by Griffiths  $et\ al.$  [38] and Grange  $et\ al.$  [73]. Lowering the LED results in smaller and narrower melt pools, leading to an increased <100> crystallographic

texture with finer columnar grains and a reduction in (HAGBs) which are common sites for micro-crack formation [38,73].

Modifying the scan strategy also influences micro-cracking. Traditional scan strategies such as 'island' or 'chess' scan strategy employed by Carter et al. [33] led to bimodal-type microstructure where micro-cracks occurred more in the overlap region of the islands. In contrast, a bi-directional scan strategy by Lam et al. [26] combined with scan rotation is effective in minimizing micro-cracking. Consistent with previous studies [38,73], this minimization was achieved by promoting a strong <100> crystallographic texture thereby minimizing the HAGBs prone to micro-cracking [26]. Additionally, re-melting strategies developed by Liu et al. [55] also minimized micro-cracking by promoting the <100> crystallographic texture. However, the positive effect of re-melting was attributed not only to the reduction in HAGBs, but also to the uniform distribution of thermal gradients and residual stresses, along with minimized segregation of elements in the grain boundaries (or interdendritic regions) [55].

Since process optimization alone cannot eliminate micro-cracks, post-processing heat treatment, particularly hot isostatic pressing (HIP), is crucial for closing or healing the micro-cracks. However, it is noteworthy that HIP does not close micro-cracks open to the surface [33,72].

Finally, some studies have indicated the presence of other micro-cracking mechanisms [58,72,74]. The identified micro-cracks did not show presence of dendritic surface or liquid films but instead had smooth surfaces and were intergranular. These were identified to be cracks that occurred in solid-state and likely strain age cracking or ductility dip cracking [58,74]. It is to be noted that these mechanisms are more commonly reported in components after post-processing heat treatment often leading to macro-cracking [75].

## 4.2. Macro-cracking

Macro-cracking refers to the millimeter-scale cracks typically formed during post-processing heat treatments. These cracks are especially observed in moderate to high  $\gamma'$  strengthened Ni-base superalloys due to the rapid  $\gamma'$  precipitation kinetics that impart additional stress along with associated changes in strength and ductility. This type of cracking is a contributing factor to making these types of alloys non-weldable in addition to the micro-cracking. There are two possible cracking mechanisms, namely strain age cracking and ductility dip cracking which will be briefly discussed here.

Strain age cracking (SAC) is a post-processing heat treatment induced macrocracking prevalent in  $\gamma'$  strengthened Ni-base superalloys. From the welding literature, it is known that this type of cracking indeed can occur during reheating in multi-pass welds [76]. However, this is unlikely the case in PBF-LB due to the high cooling rates that leads to no or very limited  $\gamma'$  precipitation [44,77,78]. Therefore, it can be agreed that SAC occurs primarily during post-process heat treatments for PBF-LB processed  $\gamma'$  strengthened Ni-base superalloys.

During post-process heat treatments two phenomena occur a) relief of residual stress and b)  $\gamma'$  precipitation. SAC occurs due to the rapid precipitation kinetics common in superalloys with higher  $\gamma'$  forming elements (Al+Ti). The rapid precipitation kinetics causes additional stresses due to the volume change associated with the formation of  $\gamma'$  which superimposed with the residual stresses from PBF-LB process, eventually leads to SAC [76]. SAC has been found to be primarily intergranular and both smooth and ductile fracture surfaces were observed [76]. It is to be noted that SAC in PBF-LB processed  $\gamma'$  strengthened Ni-base superalloys is a combination of  $\gamma'$  precipitation along with residual stress from the PBF-LB process. Therefore, they all must be addressed to certain extent to improve resistance to SAC.

Ductility dip cracking (DDC) is also a post-processing heat treatment induced macro-cracking. It has been noted that some of the Ni-base superalloys had a ductility drop in the intermediate range (700 – 900 °C) which along with the thermal strains can lead to DDC. The mechanism of DDC is reported as creep-rupture like failures where grain boundary shearing caused voids and eventually fracture. Like SAC, DDC is intergranular in nature and can occur during welding. However, possibility of occurring during PBF–LB process is limited due to the rapid cooling rates. DDC have been primarily reported for solid-solution strengthened superalloys [76]. However, there is a possibility that the drop in ductility in similar temperature range (700 to 900 °C) could be attributed to precipitation of  $\gamma'$  [45]. In fact, some of the reported macrocracks in post-process heat treated components manufactured by PBF–LB have reported both SAC and DDC mechanisms [75].

From both SAC and DDC mechanisms, it can be observed that the problem lies in the rapid  $\gamma'$  precipitation kinetics that either lead to additional stress or associated drop in ductility. Although for a particular alloy composition it is difficult to influence precipitation kinetics, there is further scope for managing the residual stress which is an identified potential research gap.

### 4.3. Microstructure and mechanical performance

The mechanical performance of an alloy is influenced by its final microstructure, which, in turn, is affected by the manufacturing and post-processing heat treatment. For instance, cast superalloys exhibit coarse grains, coarse carbides and  $\gamma/\gamma'$  eutectic [9]. In contrast, PBF–LB processed Ni-base superalloys feature fine, columnar grains, fine

carbides and limited  $\gamma/\gamma'$  eutectic [77,79]. The microstructural difference arises from the distinct thermal histories associated with the respective manufacturing processes. Achieving crack-free components via PBF–LB is critical, but the subsequent goal is attaining the required high temperature mechanical performance, particularly creep resistance.

The as-built microstructure comprises fine primary dendrites with varying elemental concentration from the dendrite core to the interdendritic region. This difference in concentration necessitates a solution heat treatment to homogenize the material before aging heat treatment. However, the first heat treatment is preferred to be hot isostatic pressing (HIP) to heal defects, such as micro-cracks, which can then be followed by a separate solutioning heat treatment [80]. In some cases, the rapid quenching possible in certain HIP equipment allows to skip the additional solution heat treatment [30].

Research has clearly demonstrated that applying heat treatments developed for conventionally manufactured (cast or wrought) superalloys to PBF–LB processed counterparts results in comparatively poor creep performance [52,68]. This highlights the need to develop tailored heat treatments specific to PBF–LB processed superalloys. For example, a recent study on Haynes 282® [52] indicated that performing higher solution heat treatment (or HIP) at 1250°C resulted in coarser grains when compared to the conventional wrought solution heat treatment at 1135 °C. This improved recrystallization and grain growth at higher temperature, increased the creep rupture life of the PBF–LB processed Haynes 282 by 3-fold compared to the wrought material. The benefit of increased solution temperature in achieving recrystallization and grain growth is also reported for other medium to high  $\gamma'$  Ni-base superalloys [51,81–83]. While coarser grains obtained through these heat treatments are generally beneficial for increasing creep rupture life [84], it has been reported that the creep performance may be anisotropic, with the longest creep rupture life observed when the specimen is loaded along the build direction [85,86].

Apart from the grain size, grain boundary elements can also influence creep performance. The critical role of boron (B) has been established in [20] where it was indicated that removing B led to poor creep performance, while [19] indicated that increasing B above the standard levels resulted in improvement of creep performance in both, along and transverse to the build direction. This difference is attributed to the formation of borides which supply B to the grain boundary, improving grain boundary cohesion. These studies indicate that microstructure tailoring either through alloy design and post-processing heat treatments can improve creep performance to match or approach the conventional counterparts. However, attempts to influence the microstructure directly through PBF-LB processing and the subsequent influence on creep performance remain limited.

### 5.1. Material

The CM247LC powder used in this thesis was VIGA powder provided by Höganäs AB (Höganäs, Sweden). The powder had a particle size range of 15 to 45  $\mu$ m which was sieved in subsequent prints using a 63  $\mu$ m sieve. The chemical composition, as provided by the supplier, is shown in *Table 2*.

**Table 2.** Chemical composition of the standard CM247LC powder used in Paper I – Paper VII

	$\mathbf{Cr}$	Co	Mo	С	W	Hf	Ta	Ti	Al	$\mathbf{Zr}$	В	Ni
$\mathrm{wt.\%}$	8.00	9.30	0.50	0.06	9.70	1.30	3.20	0.80	5.60	0.009	0.010	Bal.

Two powder additives were prepared to modify the base CM247LC composition and were studied in Paper I. These were prepared by using the standard CM247LC powder as the base and adding either 1 wt.% nano-Y<sub>2</sub>O<sub>3</sub> or 1 wt.% Hf mixed in a slow mixer for 4 hours. These additives, sourced from US Research Nanomaterials Inc. (Houston, TX, USA), had particle size ranges of 20 to 45 nm for nano- Y<sub>2</sub>O<sub>3</sub>, and 30 to 45 μm for Hf. However, the remainder of the appended papers utilized the standard CM247LC powder without any chemistry modification.

Paper VIII used powder sourced from another supplier and the composition is shown in  $Table \ 3$ .

Table 3. Chemical composition of the standard CM247LC powder used in Paper VIII

	$\mathbf{Cr}$	$\mathbf{Co}$	Mo	$\mathbf{C}$	$\mathbf{W}$	Hf	Ta	${f Ti}$	Al	${f Zr}$	В	Ni
$\mathrm{wt.}\%$	8.25	9.23	0.60	0.07	9.53	1.35	3.01	0.74	5.5	0.013	0.018	Bal.

## 5.2. PBF-LB process

The specimens in Paper I were printed using a miniaturized PBF–LB machine (miniSLM) developed at Paul Scherrer Institute (PSI) in Switzerland for using in a synchrotron beamline and more information can be found elsewhere [87,88]. This machine was used for operando X-ray radiography (imaging) experiments at the TOmographic Microscopy and Coherent rAdiology experimenTs (TOMCAT) beamline of the Swiss Light Source (SLS) at PSI in Switzerland.

The specimens in Paper II – Paper VIII were printed using a commercial EOS M290 machine (Electro Optical Systems GmbH, Krailling, Germany). This machine is equipped with Yb-fiber laser having a gaussian intensity distribution and a spot diameter at the focal plane of  $\sim 85$  to  $100~\mu m$ . The laser was operated in continuous

wave mode. The PBF–LB process was carried out in a chamber where the oxygen level was maintained below 0.1% with continuous flow of Argon gas to minimize oxidation. All the specimens utilized a bi-directional scan strategy, and additional details can be found in the appended papers. Table 4 indicates the process parameters used for the baseline specimens used in Paper V – Paper VII. This parameter is optimized to have the lowest micro-cracking. The specimens were separated from the build platform using a bandsaw or EDM before further analysis or heat treatment.

Table 4. Baseline parameter used in Paper V- Paper VII

Power	Speed	Hatch	Layer thickness
(W)	$(\mathrm{mm/s})$	(mm)	(mm)
125	1200	0.05	0.03

### 5.3. Heat treatment

The heat treatment consisted of hot isostatic pressing (HIP) that was combined with solution heat treatment, performed in a Quintus QIH21 HIP with molybdenum furnace at Quintus Technologies AB (Västerås, Sweden). The HIP temperatures were in the range of 1250 °C to 1280 °C performed for 4 hours with pre-pressurisation strategy of 200 MPa (see Section 6.2.2). The specimens then were aged in a TAV H4-S type industrial vacuum furnace (TAV Vacuum Furnaces SPA, Caravaggio BG, Italy) which was performed at 871 °C for 20 hours.

## 5.4. Metallographic preparation

Specimens for metallographic preparation were extracted parallel or transverse to the build direction. Specimens that required sectioning were cut using an abrasive disc on a Buehler IsoMet High Speed Pro precision cutter. This was followed by mounting the specimens in conductive Struers Polyfast resin (Struers ApS, Ballerup, Denmark). The mounted samples were then followed by successive grinding steps using SiC papers ranging from 320 to 4000 grit size on a Struers Tegrapol. This was followed by polishing using a diamond suspension of 3 µm on a taffeta woven wool surface (MD-Mol by Struers) and then a 1 µm polishing. After this, the mounted specimens were suitable for defect analysis using optical microscopy. However, an additional polishing step using 0.05 µm colloidal silica polishing was done before high-resolution scanning electron microscopy or etching.

Two types of etchants were utilized -1) immersion/swab etching using Kalling's 2 (5g cupric chloride + 100 ml 37% hydrochloric acid + 100 ml ethanol) or 2) electrolytic etching using 10 wt.% phosphoric acid or 10 wt.% oxalic acid at 3 to 5 V for 5 to 10 seconds. The choice of the etchant was more important for SEM than OM. Kalling's 2 etched the interdendritic region or the  $\gamma'$  precipitates, while the electrolytic etching

etched the dendritic core or the  $\gamma$  matrix. A comparison of the microstructures (as-built and heat-treated) using the two etchants for CM247LC is shown in *Figure 6*.

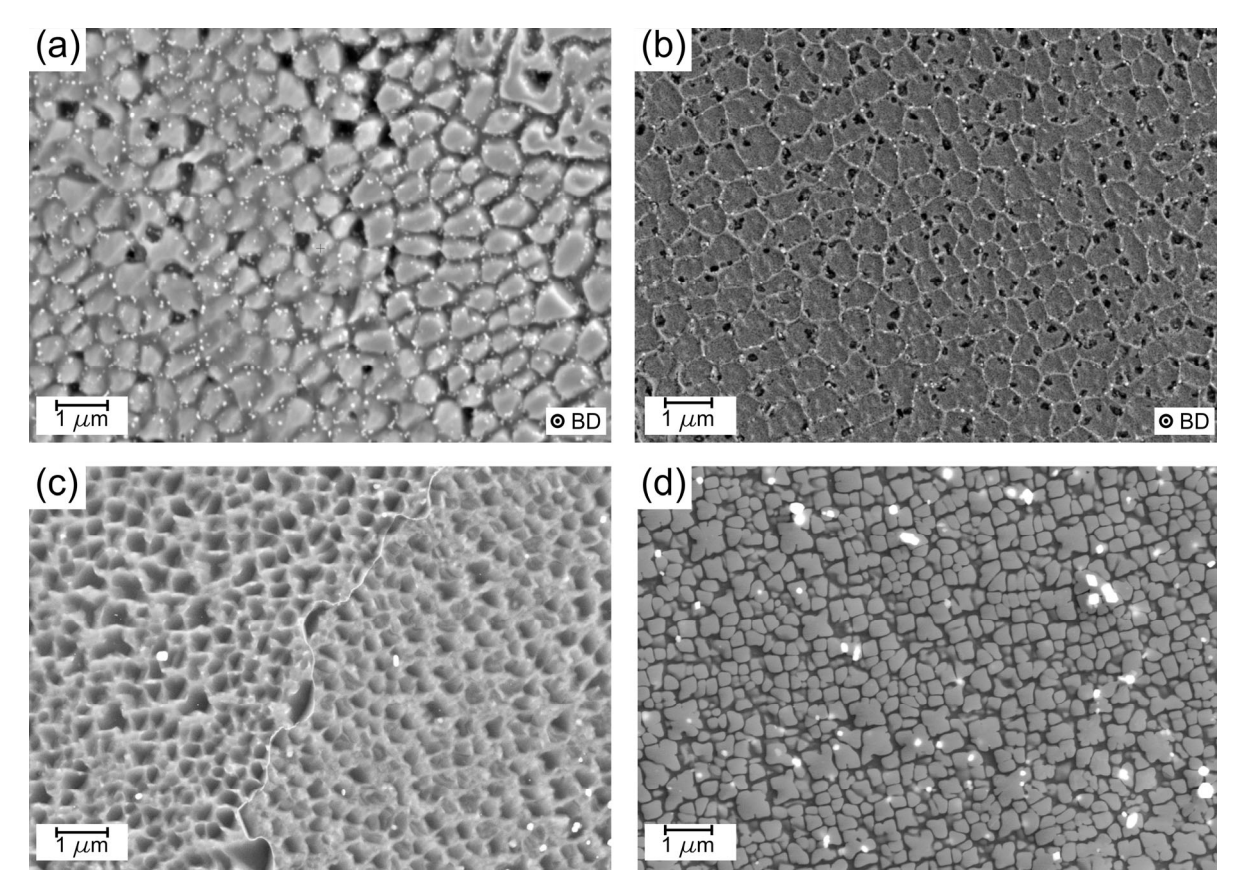


Figure 6. Comparison of etched microstructures (a), (c) Etched with Kalling's 2, (b), (d) Electrolytical etching with 10 wt.% oxalic/phosphoric acid. (a), (b) As-built microstructure. (c), (d) Heat-treated (HIP+age) microstructure. (a)-(c) Obtained in SEM with SE detector. (d) Obtained in SEM with BSE detector.

## 5.5. Optical Microscopy

The metallographically prepared samples before etching were analyzed using optical microscopy (OM) performed mostly using a Zeiss Axiovision 7 (Carl Zeiss Microscopy GmbH, Oberkochen, Germany). This microscope has a motorized stage which was used to obtain stitched micrographs of the entire cross-section to analyze defects (cracks and porosity). This microscope was also used for observation of solidification microstructures, particularly melt pools after etching. The macro-cracking on cruciform was observed using a Zeiss Stereo Discovery.V20 stereo optical microscope (SOM).

## 5.6. Scanning Electron Microscopy

The scanning electron microscopy (SEM) was performed using either a Zeiss Leo Gemini 1550 or a Zeiss Gemini 450 (Carl Zeiss Microscopy GmbH, Oberkochen, Germany) which were equipped with similar detectors and had a field emission gun (FEG) electron source. Metallographically prepared samples, fracture surfaces and powders were analyzed using SEM.

## 5.6.1. SEM imaging and chemical analysis

Imaging was performed using different detectors, namely secondary electron (SE), backscattered electron (BSE) and in-lens detector. The SE detector was used to observe the etched microstructure or to observe fracture or crack surfaces. The in-lens detector was used to observe the microstructure specifically at high magnifications. The BSE detector was used to observe chemical contrast in the microstructure, both in etched and unetched conditions. The BSE detector was also used to observe microstructures due to its sensitivity to crystallographic orientation contrast. The accelerating voltages used for imaging ranged from 5 to 10 kV. The current in Zeiss Gemini 450 was typically  $\leq$ 500 pA, while aperture of 30 µm or 60 µm was used in Zeiss Leo Gemini 1550.

Energy dispersive spectroscopy (EDS) was performed using either Ultim-Max or X-Max EDS detector (Oxford Instruments, Abingdon, Oxfordshire, England). EDS provided elemental composition of the phases or features observed in SEM which were obtained from a point, line scan or a map. EDS acquisition was performed using an accelerating voltage of 10 to 20 kV, probe current of 2 to 5 nA and working distance of ~8.5 mm.

#### 5.6.2. Electron backscattered diffraction

Electron backscattered diffraction (ESBD) was performed using either Nordlys II or Oxford Symmetry EBSD detector (Oxford Instruments). EBSD acquisition was performed using an accelerating voltage of 20 to 30 kV and probe current of 2 to 10 nA. The acquired data underwent basic clean-up in Aztec Crystal consisting of removing wild spikes and zero solution removal ranging from 8 to 5 nearest neighbors. The EBSD maps in inverse pole figure (IPF) representation and pole figures were plotted using open source MTEX toolbox (version 5.9.0) [89] in MATLAB®.

## 5.6.3. Electron channeling contrast imaging

Electron channeling contrast imaging (ECCI) is an SEM-based characterization performed using the BSE detector that allows to image crystal defects such as dislocations, stacking faults and twins. The relationship between the incident electron beam and the varying crystal lattice orientation leads to difference in the backscattered electron intensity. ECCI is best performed in a grain/region that appears dark, and the crystal defect would have a higher BSE intensity. However, controlled ECCI (cECCI) uses orientation information from EBSD to go into the two-beam diffraction conditions [90].

ECCI and cECCI micrographs presented in this thesis were obtained using Zeiss Gemini 450 with accelerating voltage of 20 to 30 kV, probe current of 2 to 5 nA and working distance of 5 to 8 mm. For cECCI, the region of interest was first observed with the BSE detector and eucentric height was achieved. Following this the EBSD

was performed on the region of interest, and the orientation information was obtained. This information is then used in the commercial computer program TOCA v2.3 (Tools for Orientation Determination and Crystallographic Analysis, initially developed by S. Zaefferer, now acquired and commercially distributed by Zeiss) [90,91]. This software is then used to tilt and rotate the specimen to go into the required two-beam condition for the cECCI.

## 5.7. Atom probe tomography

The atom probe tomography (APT) measurements were performed using the local electrode atom probe LEAP 6000 XR from CAMECA (Madison, Wisconsin, US). The instrument was used in laser pulse mode at 50 K specimen temperature, 0.5 to 3% evaporation rate and 30 to 35 pJ laser energy. Reconstructions were made in the commercial software AP Suite 6.3 (CAMECA). The samples were prepared either through electrolytic polishing [92] or through focused ion beam-SEM FEI Versa 3D workstation through standard lift-out procedures [93].

# 5.8. X-ray diffraction

Diffraction based techniques such as X-ray diffraction (XRD) are routinely used for phase identification and texture determination. The principle of diffraction is based on Bragg's law of diffraction as shown in Eqn. 3. The incident X-rays interact with the crystal lattice and undergo constructive interference as shown Figure 7 and a diffraction peak is obtained.

$$n\lambda = 2d_{hkl}\sin\theta \tag{3}$$

where n is an integer,  $\lambda$  is the wavelength of the X-ray,  $d_{hkl}$  is the interplanar spacing of hkl planes and  $\theta$  is the Bragg's angle.

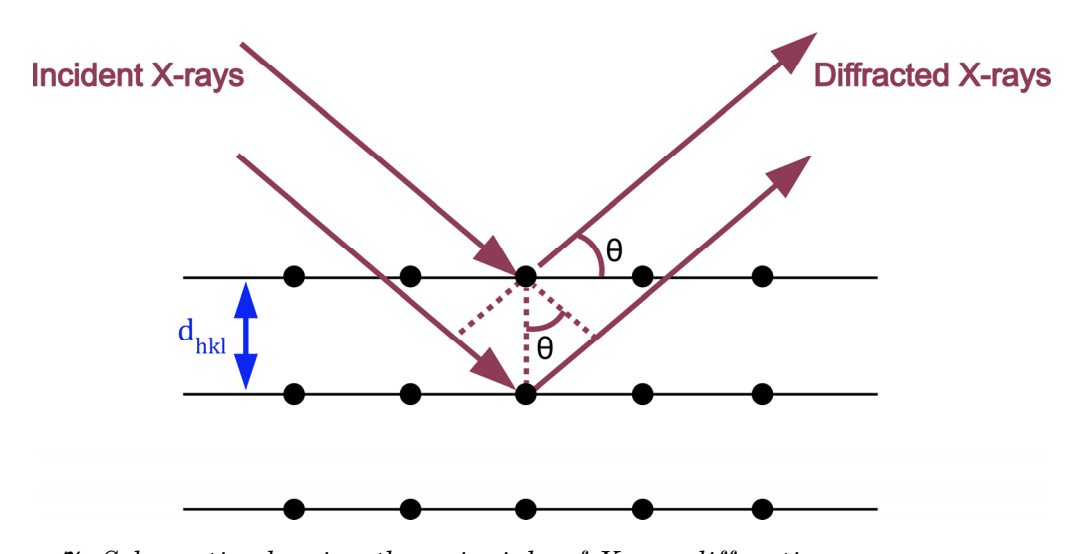


Figure 7. Schematic showing the principle of X-ray diffraction.

In this thesis XRD has been used primarily for measuring residual stress on PBF-LB processed samples. Table 5 summarizes the XRD equipment used in this thesis. The  $\sin^2 \psi$  method was used for the evaluation of residual stress [94] assuming quasi-isotropic elastic material behavior and plane stress (i.e.  $\sigma_{33}=0$ ) The measurements were performed on the lateral surface of the sample along the vertical direction (// to BD) and horizontal direction ( $\perp$  to BD) in varying  $\psi$  ranges. Because of the limited penetration depth of X-rays, electrolytic etching was performed to obtain a depth profile until  $\approx 200$  µm in Paper II – Paper IV. However, no electrolytic etching was performed in Paper V due to the higher penetration depth of Synchrotron X-rays. The energy dispersive nature of the white beam synchrotron X-ray used in Paper V also provides residual stress information for higher depths (up to  $\approx 50$  to 100 µm). Subsequent data analysis was performed for peak fitting and residual stress calculation using X-ray diffraction elastic constant (DEC) which can be found in Paper II – Paper V.

**Table 5**. Summary of XRD equipment used in this thesis

Paper	Equipment	Source
Paper II	Seifert X-ray diffractometer	Cr X-ray tube
Paper III	LIMAX-160 X-ray diffractometer at	Liquid Ga MetalJet
	Helmholtz Zentrum Berlin (HZB)	(Energy dispersive)
Paper IV	Stresstech G3 mobile diffractometer	Mn X-ray tube
Paper V	P61A beamline at Deutsches Elektronen-	Synchrotron white beam
	Synchrotron (DESY)	(Energy dispersive)

#### 5.9. Creep testing

All the creep tests were performed in fully heat-treated conditions consisting of HIP + aged as mentioned in Section 5.3. The creep tests were performed at temperature of 871 °C and 380 MPa and creep strains were measured. In Paper VII, the creep test was performed as dead weight creep utilizing a Bofors test frame [95] equipped with a purpose-built furnace from Entech (Entech Energiteknik AB, Ängelholm, Sweden). The creep strain was noted manually at fixed time increments, and the test was carried in accordance with ISO 204:2018. In Paper VIII, an electromechanical creep testing system (ZwickRoell KAPPA 050 DS, Ulm, Germany) equipped with the ZwickRoell universal 3-zone furnace, following the ISO 204:2009, was used. The creep strain was measured using a rod-and-tube extensometer clamped to the test piece's collar. All creep tests were performed until fracture, and the results were compared on a Larson–Miller Parameter (LMP) plot. LMP is given by (T + 273)\*(20 + log10(t))/1000, where T is the temperature in °C and t is the creep life in hours.

## 6. Summary of results

This thesis is based on the results from the eight appended papers (Paper I – Paper VIII) along with some complementary results. The primary objective is to understand the effects of PBF–LB processing and post-processing heat treatment on microcracking, macro-cracking and creep performance of CM247LC, supported by microstructure and residual stress characterization.

In Paper I, synchrotron X-ray radiography and SEM analysis were used to establish the micro-cracking mechanism. This paper also presents and discusses micro-crack mitigation pathways in CM247LC with additions of either Hf or nano- $Y_2O_3$ . Paper II – Paper IV deals with optimizing PBF–LB process parameters and scan strategies to control micro-cracking, microstructure and residual stresses. Complementary results on macro-cracking are also presented here for Paper II and Paper III. Paper V elucidates the  $\gamma'$  precipitation and residual stress relief with intermediate heat treatment to understand the macro-cracking mechanism. Paper VI presents how post-process heat treatment, particularly standard and modified HIP (pre-pressurisation) strategies influence micro-cracking, macro-cracking and microstructure. Paper VII presents how the temperature in HIP using pre-pressurisation strategy influence microstructure and creep performance. Paper VIII reveals how the optimized PBF–LB process induced anisotropic microstructure improves creep performance.

## 6.1. Micro-cracking

#### 6.1.1. Micro-cracking mechanism

A primary challenge in the PBF–LB processing of CM247LC is the consistent formation of micro-cracks. Through a combination of real-time synchrotron X-ray radiography and detailed post-mortem SEM/EBSD observations, the mechanism of micro-cracking was identified. Both observations confirmed that micro-cracks occur during the final stages of the solidification process, aligning with the mechanism of solidification cracking. SEM/EBSD observations indicated that the crack surfaces had evidence of dendritic structures from solidification and found at HAGBs with misorientation  $\geq 15^{\circ}$ . Section 6.1.2 will briefly present the different micro-crack mitigation strategies.

## 6.1.2. Micro-cracking mitigation

The first route explored the addition of elemental or oxide powders to the CM247LC powder to alter the solidification path. Both additions of 1 wt.% Hf or 1 wt.% nano- $Y_2O_3$  were successful in minimizing micro-cracking (Paper I). For the Hf-added sample, the partial melting of high-melting point Hf particles increased the availability of liquid in the interdendritic regions during the terminal stages of solidification. This enhanced

liquid feeding aids in backfilling, thereby minimizing the micro-cracking. However, with the  $Y_2O_3$ -added sample, the radiographs revealed a reduction in melt pool depth. This effect leads to a smaller volume of solidifying material and was crucial for reducing micro-cracking and provided a direct connection to the beneficial effects later explored through PBF-LB process optimization.

Process optimization proved to be a relatively scalable and effective strategy for tailoring melt pool geometry and solidification to minimize micro-cracking. The initial work (Paper II) established that linear energy density (LED) is a critical factor in controlling micro-cracking, unlike volumetric energy density (VED), which did not correlate well with micro-cracking. Low LED ( $\sim 0.1 \text{ J/mm}$ ) processing resulted in low micro-cracking, while high LED ( $\geq 0.2 \text{ J/mm}$ ) led to severe micro-cracking (Figure 8). The positive effect of low LED is primarily attributed to a lower fraction of HAGBs, the known locations of micro-cracking. To prevent lack of fusion defects when using low LED, it is crucial to have smaller hatch spacing ( $\sim 50 \text{ µm}$ ).

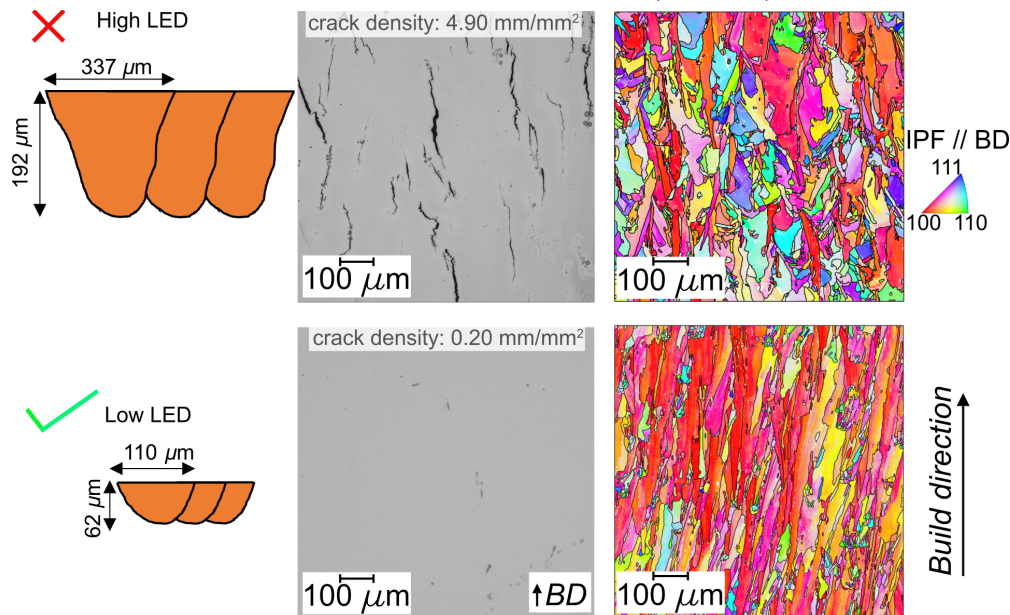


Figure 8. OM and EBSD map in IPF representation with superimposed HAGBs along with schematic of representative melt pool shape and size.

Beyond energy input, scanning strategies were also found to influence micro-cracking. Processing with scan rotation of  $67^{\circ}$  or  $90^{\circ}$  successfully minimized the severe anisotropic micro-cracking seen in samples with no rotation  $(0^{\circ})$ , as shown in Paper IV. The reason for the increased micro-cracking for no rotation is attributed to the long columnar grains with HAGBs. Additionally, Paper III and Paper IV indicated that both stripe scan and re-melting strategies minimize micro-cracking. In all the samples with low micro-cracking, two consistent features observed are: 1) narrow and shallow melt pools and 2) columnar grains with <100> crystallographic texture along the build direction. Narrow and shallow melt pool is an indication that smaller volume of material is

melted, which has lower shrinkage during solidification. And the resulting columnar microstructure allows for better liquid feeding in the interdendritic region during terminal stages of solidification.

Critically, none of the PBF–LB processes investigated could eliminate micro-cracking. This highlights the necessity of post-processing techniques such as HIP (Paper VI), to heal the residual micro-cracks and achieve full material density. However, macro-cracking occurs during post-processing heat treatment; the mechanism and mitigation of macro-cracking is summarized in *Section 6.2*.

## 6.2. Macro-cracking

## 6.2.1. Macro-cracking mechanism

Macro-cracking, which is observed after post-processing heat treatment, is a major hindrance for industrial adoption of PBF-LB processing of CM247LC. To better understand the temperatures at which these macro-cracks occur and the associated microstructural changes, isothermal heat treatments ranging from 650 to 1050 °C for 1 to 8 hours were performed (Paper V). Emphasis was placed on characterizing the evolution of  $\gamma'$  precipitation for the different heat treatments using SEM and APT, with the as-built condition serving as a reference. APT results indicated that the asbuilt material contain clusters of Cr-rich and Cr-depleted (Al-rich) regions, which suggests early stages of spinodal decomposition [96]. With further heat treatments, the Cr-rich and Al-rich regions become further enriched with the respective elements, and  $\gamma'$  precipitates are observed at temperature of  $\geq 750$  °C. However, the macro-cracks formed under this condition is linked to the formation of  $\gamma'$  precipitates aligning with the strain age cracking (SAC) mechanism. SAC is dependent on γ' precipitation kinetics and residual stresses from the PBF-LB process. Since precipitation kinetics cannot be influenced without alloy modification, mitigation efforts are focused on minimizing residual stress (and thus SAC) through PBF-LB processing or postprocessing heat treatments.

#### 6.2.1. Macro-cracking mitigation

Residual stresses were found to be strongly influenced by PBF–LB process parameters, including scan strategies. VED influenced the sub-surface residual stress along the build direction (Paper II). Interestingly, two samples with completely different parameters but same VED exhibited similar maximum residual stresses (~1000 MPa) at a depth of 200 µm. While processing with low VED is found to give relatively low residual stress (~800 MPa), this was at the expense of higher lack of fusion defects, necessitating alternative routes for residual stress minimization. It should be noted that the high residual stress values reported in Paper II are attributed to the specific

choice of the diffraction plane and diffraction elastic constant, which was corrected in the subsequent papers.

Scan rotation strategies influenced sub-surface residual stresses and macro-cracking in a complex manner (Paper IV). The lowest degree of macro-cracking was observed when no scan rotation strategy was applied, despite having residual stress levels (~600 to 700 MPa) similar to the scan rotation samples (67° or 90°) that macro-cracked severely. This difference in macro-cracking is attributed to the anisotropic residual stress state induced along the scanning direction for the no scan rotation sample [97], which caused the macro-cracking to shift away from the stress concentrators and localize on the top of the cruciform. Conversely, re-melting strategies were found to be disadvantageous (Paper IV), resulting in higher residual stresses (~700 to 800 MPa) and increased macro-cracking. Interestingly, varying stripe width provided promising results as the sub-surface residual stress decreased with the decrease in stripe width (Paper III). The 0.2 mm stripe width yielded the lowest residual stress (~650 MPa), and did not undergo macro-cracking, when compared with the 5 mm stripe width (~850 MPa) which macro-cracked (Figure 9).

These results collectively indicate that the optimal strategy to mitigate SAC is to not merely minimize residual stress along a single direction, but rather to utilize scanning strategies to influence the residual stress state near critical locations such as stress concentrators.

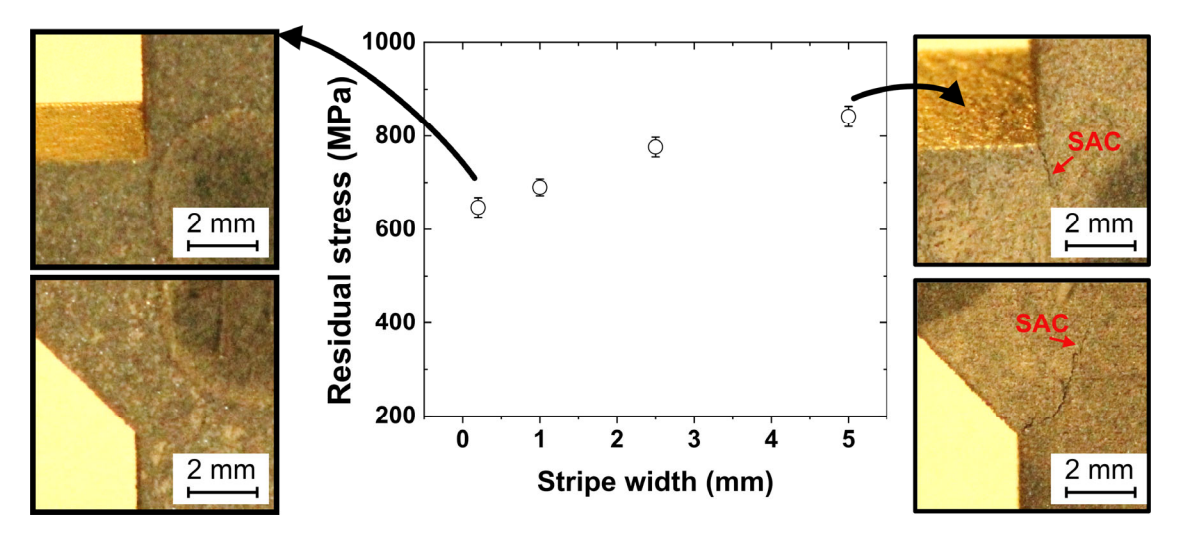


**Figure 9**. Sub-surface residual stresses measured using lab-XRD after electropolishing 50 μm along with macro-cracking (indicated by SAC) observation on cruciform after HIP for different stripe widths. Note that the instrument used for measurements is an energy dispersive diffractometer LIMAX-160 at HZB, Germany.

### 6.2.2. Macro-cracking mitigation by heat treatment

Hot isostatic pressing (HIP) strategies were investigated as a post-processing step to minimize macro-cracking on the baseline samples (Paper VI). Two HIP approaches, Standard and Pre-pressurisation, were tested. The Standard strategy ramps both the temperature (1250 °C – 1280 °C) and pressure (100 MPa) simultaneously and in pre-pressurisation strategy the pressure was ramped to targeted pressure (200 MPa) followed by the ramp to the targeted temperature (1250 °C – 1280 °C). The schematic representation of the HIP strategies is shown in Figure~10~(left). The macro-cracking (SAC) observations (Figure~10~(center)) on the mechanical test specimens indicated that the pre-pressurisation strategy eliminated macro-cracking. However, macro-cracking occurred in the cruciform geometry as shown in Figure~10~(right). This suggests that while additional pressure aids in minimizing macro-cracking, its effectiveness is geometry dependent and does not guarantee elimination in components with stress concentrators. Therefore, tailored heat treatments involving holding at a lower temperature for obtaining stress relief was investigated.

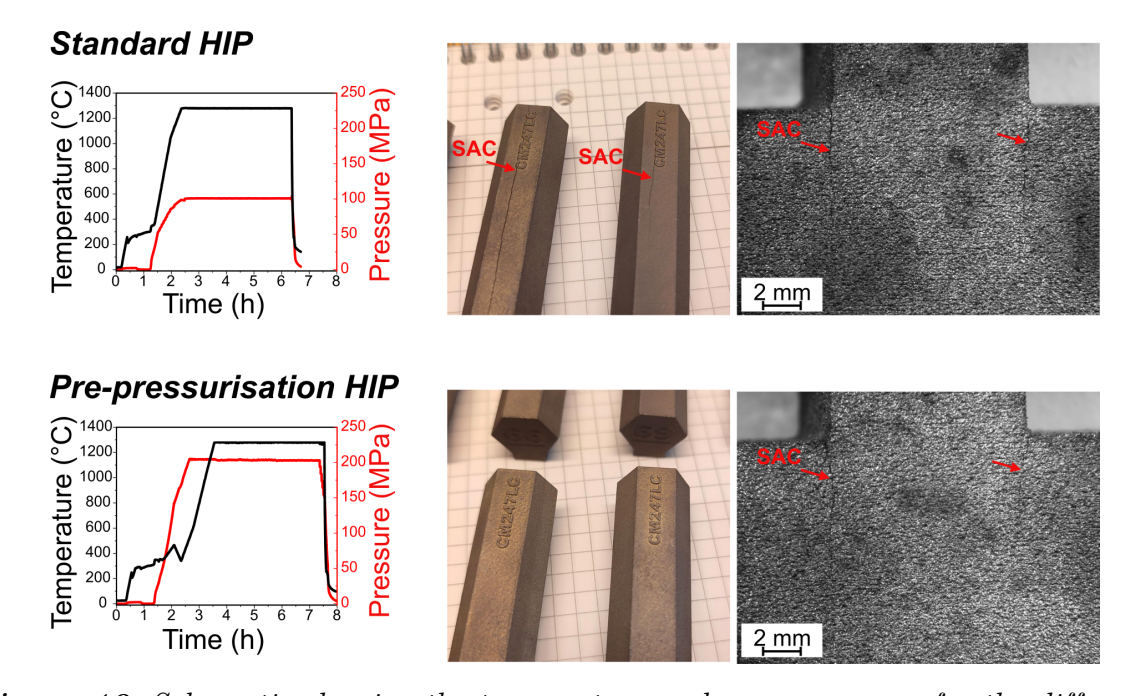


Figure 10. Schematic showing the temperature and pressure ramp for the different HIP strategies along with macro-cracking (indicated by SAC) observations on mechanical test specimens (center) and cruciform (right) post-HIP.

Screening for this potential stress relief window involved heat treatments at intermediate temperatures, coupled with macro-crack observations and sub-surface residual stress measurements using synchrotron white beam XRD without electropolishing (Paper V). The residual stress value reported in Paper V are lower than Paper II – Paper IV, because they are obtained from a depth of ~40 µm using the (311) diffraction plane. The results indicated no stress relief at 650 °C (~475 MPa) and

minimal stress relief at 700 °C (~350 MPa), with longer holding times having no further influence at these temperatures. Although holding at 750 °C provided significant stress relief, however, this was accompanied by macro-cracking. This ultimately demonstrates that significant residual stress relief was not achieved without triggering  $\gamma'$  precipitation and subsequently macro-cracking.

## 6.3. Creep performance

## 6.3.1. Impact of PBF-LB process

The influence of PBF-LB process parameters on the resulting heat-treated microstructure is shown in Figure 11 (top). To facilitate comparison across varying parameters, VED is used as a unifying metric. Among the conditions shown are optimized conditions indicated in Figure 11b,d with lowest micro-cracking for respective layer thicknesses. Figure 11a, c are non-optimal conditions with higher fraction of lack of fusion and micro-cracking, respectively. It is important to note that despite using non-optimal PBF-LB conditions, the subsequent HIP treatment successfully produced high density samples (> 99.9%).

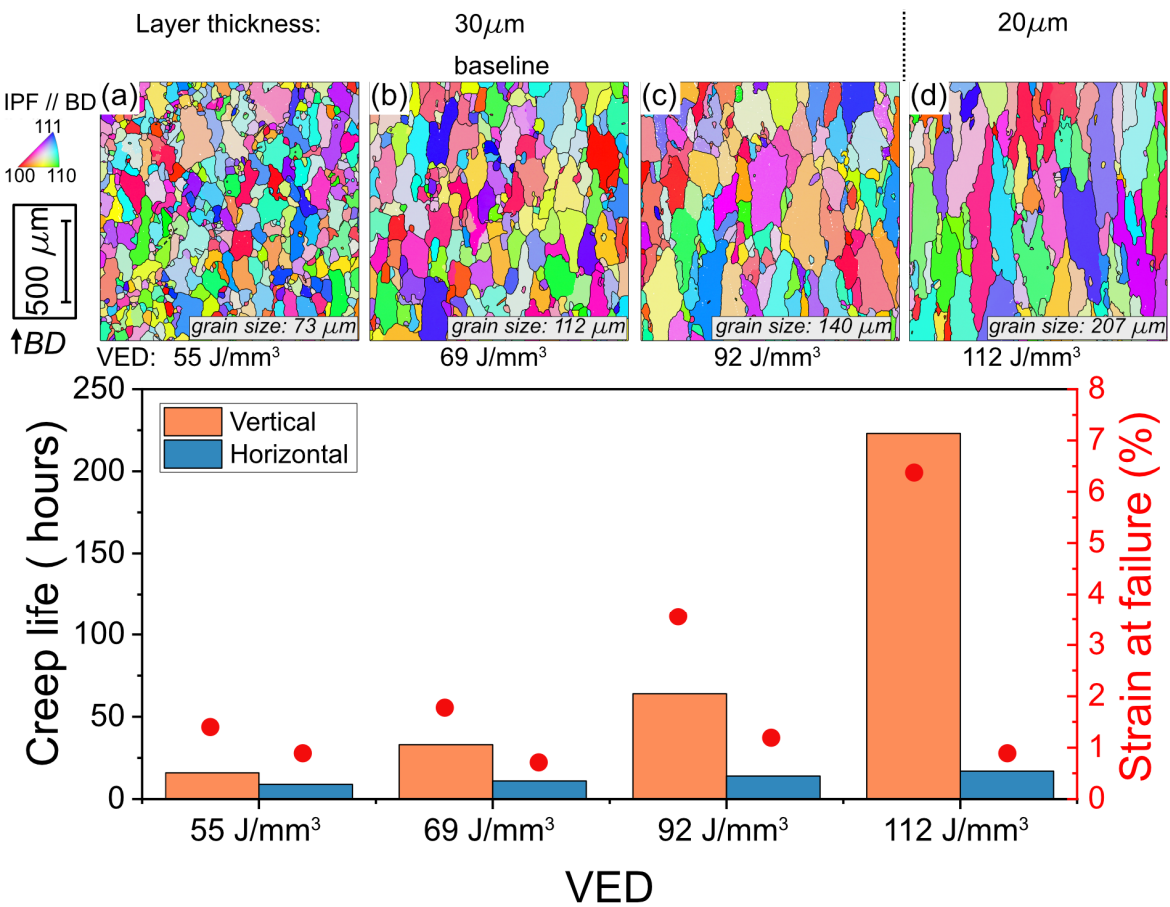


**Figure 11**. (Top) EBSD orientation map in IPF representation along the build direction for samples with different VED and same heat treatment (HIP + age). (Bottom) Creep life and strain at failure for sample tested at 871 °C/380 MPa for the same samples in vertical and horizontal direction. Grain size is the average of the fitted ellipse major diameter.

The results indicate that the microstructure transitions from near-equiaxed to columnar microstructure with the increasing VED. The average grain size in terms of fitted ellipse major diameter increases from 73 µm to 207 µm with the VED; however, the sample with the highest VED has grains that are nearly 1 mm long. The microstructure evolution correlates directly with creep performance, as shown in Figure 11 (bottom). The creep life and strain at failure increase significantly with VED, particularly along the vertical direction. The notable improvement in the creep performance is attributed to the columnar grains being aligned along the build direction. The best creep life is achieved for the highest VED condition (223 hours), while the lowest VED performed the worst (16 hours). Interestingly, the non-optimal condition (VED of 92 J/mm³) had twice the creep life when compared to the optimal baseline. In general, the vertical specimens (Figure 11b-c) exhibited longer tertiary creep stage and presence of creep voids and cracks, reflecting widespread plasticity (Paper VII and Paper VIII).

In contrast, the creep performance of the horizontal specimens was consistently poor (creep life: ~10 to 20 hours and strain at failure: <1%). The creep curves and quantification of creep damage indicated a limited tertiary creep stage. Further characterization revealed that the horizontal creep specimens have limited plasticity, confirming they undergo premature facture. The poor creep performance in horizontal specimen is attributed to the unfavorable orientation of grain boundaries that facilitates easier crack initiation and propagation. Therefore, further efforts must be placed on increasing grain size and achieving interlocking grains to avoid this easy crack propagation path.

#### 6.3.2. Impact of heat treatment

The choice of HIP temperature is found to impact both the microstructure and the resulting creep performance. Initial results (Paper VI) indicated that HIP temperature (1250 to 1280°C) and strategy (Standard or Pre-pressurisation) did not significantly affect the microstructure (grain size and precipitates). However, a follow-up study (Paper VII) comparing the 1250°C and 1280°C HIP using pre-pressurisation strategy (+ aged) revealed a slight but notable difference in the creep life for the vertical specimens. Specifically, the higher temperature HIP at 1280°C resulted in 23% longer creep life in comparison to the 1250°C HIP condition. This improvement in creep performance is attributed to a combination of the following microstructural differences in the two conditions:

 Grain size: The 1280°C HIP resulted in a 15% increase in distribution of larger grains (fitted ellipse major diameter) in the 100 – 200 μm range, compared to the 1250 °C HIP.

- γ' precipitate size/morphology: The 1280 °C HIP condition produced finer, cuboidal-shaped γ' precipitates (average size: 274 nm) indicating superior γ' solutioning. In contrast, the 1250 °C HIP condition had coarser and irregularly shaped precipitates (average size: 340 nm), as shown in *Figure 12*.
- Grain boundary decoration: Figure 12 illustrates that the 1280 °C HIP lead to finer and more distributed borides along grain boundaries compared to the blocky borides for the 1250 °C HIP. The increased presence of borides at the grain boundaries in the 1280 °C HIP condition is attributed to the improved  $\gamma'$  solutioning.

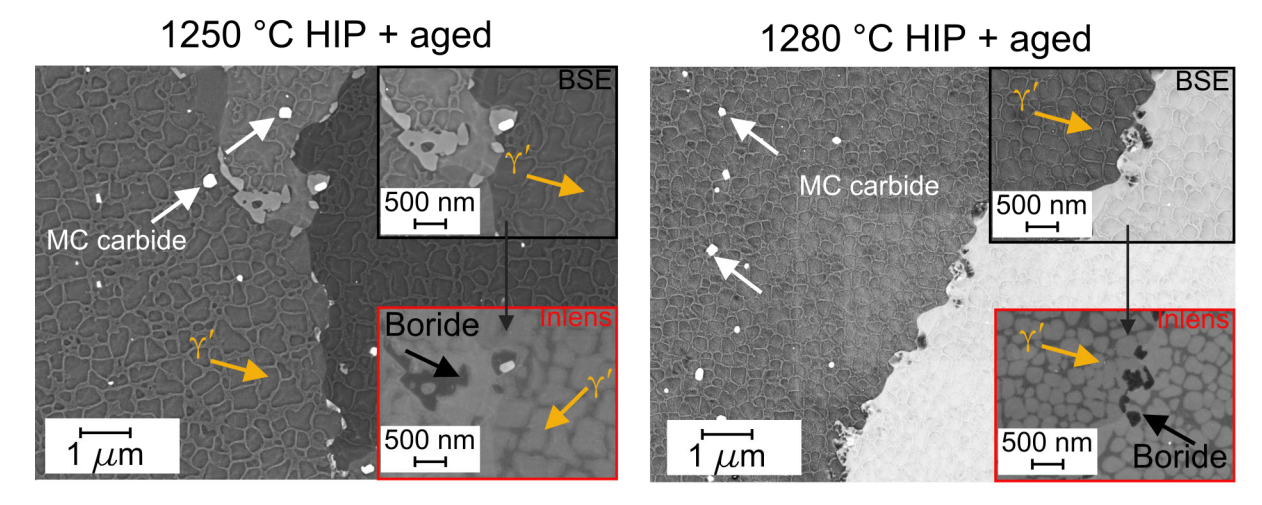


**Figure 12**. Microstructure of HIP+aged samples for HIP temperatures of 1250 °C and 1280 °C using the pre-pressurisation strategy. Build direction is from the bottom to top in the micrographs.

# **RQ1**: What is the mechanism of micro-cracking during PBF-LB processing of CM247LC, and how can it be mitigated?

- The micro-cracking observed in PBF–LB processed samples is solidification cracking and is usually found at high-angle grain boundaries with misorientation > 15°.
- Additions of either 1 wt.% Hf or 1 wt.% nano-Y<sub>2</sub>O<sub>3</sub> particles reduce microcracking by altering the melt pool depth, solidification pathway, and undergo distinct metallurgical reactions. For Hf-added powder, partial melting of Hf particles aided in increased segregation to interdendritic region thereby reducing micro-cracking. For Y<sub>2</sub>O<sub>3</sub>-added powder, formation of (Hf, Ta, Al, Y) oxide and reduction in melt pool depth was observed, with the latter attributed to aid in minimizing micro-cracking.
- Processing with shallow and narrow melt pools either by lowering LED, short stripe width, or re-melting strategies minimized micro-cracking.
- The advantage of shallow and narrow melt pool is attributed to the smaller melted volume that leads to lower shrinkage during solidification; the resulting microstructure had columnar <100> oriented grain structure with lower fraction of HAGBs.
- Process optimization allowed to minimize micro-cracking but does not eliminate it. This indicates the necessity of post-processing heat treatment, particularly HIP, to heal the residual micro-cracks.
- HIP heals micro-cracks present in the bulk of the sample, but micro-cracks open to the surface cannot be healed.

# **RQ2**: What is the mechanism of macro-cracking during post-processing heat treatment of PBF-LB processed CM247LC, and which factors influence it?

- The macro-cracking observed in PBF-LB processed samples is linked to  $\gamma'$  precipitation aligning with the strain age cracking mechanism. The macro-cracks were typically observed near stress concentrators.
- Lowering residual stresses by either processing with lower VED, or short stripe width is a potential route to lower macro-cracking.
- Performing HIP with the higher pressure (200 MPa), particularly applying the *pre-pressurisation* strategy, lowers macro-cracking. However, macro-cracking is also observed to be dependent on geometry (size and shape).

- Heat treatment at temperatures of 700 °C up to 4 hours resulted in partial stress relief without causing macro-cracking. Heat treatments of ≥ 750 °C resulted in more effective stress relief but concurrently caused macro-cracking.
- Only one of the explored strategies involving short stripe width can eliminate macro-cracking. However, this is a slower process indicating the need for further research to influence residual stress distribution.

# **RQ3**: How does PBF–LB processing and heat treatment affect the microstructure and creep performance of CM247LC?

- The microstructure is heavily dependent on the PBF–LB process parameters. Increasing the energy density (VED or LED) is a possible way of transitioning from equiaxed to columnar grains.
- The overall creep performance of PBF–LB processed CM247LC is inferior compared to the cast CM247LC from the investigated PBF–LB processing and post-processing heat treatments.
- The creep performance improved along the vertical direction for columnar microstructure (grain length up to 1 mm) by using either higher energy input or lower layer thickness, approaching the performance of cast CM247LC.
- The horizontal creep performance is consistently poor and cannot be influenced by PBF-LB processing. The poor creep performance of horizontal specimens is attributed to the unfavorable orientation of grain boundaries that facilitate easier crack formation and propagation leading to anisotropic creep performance.
- HIPing at 1280 °C led to a 23% improvement in creep rupture life along the build direction in comparison to the 1250 °C HIP condition. This improvement is connected to coarser grains, finer γ' precipitates and enhanced grain boundary decoration with borides, resulting from improved solutioning.

### 8. Future work

The benefits of admixed hafnium in minimizing micro-cracking were established (Paper I). Future work should move beyond admixing to investigate the influence of an increased Hf content (1.5 - 2 wt.%) in a pre-alloyed condition. This study is essential to understand this effect on heat-treated microstructure and overall performance, specifically regarding micro-cracking, macro-cracking susceptibility, and high-temperature creep response. Additionally, the impact of key grain boundary strengthening elements, such as boron (B) and zirconium (Zr), on the microstructure and high temperature performance, is of interest.

Current PBF–LB processing was performed exclusively using a gaussian laser beam (~85 to 100 µm spot size). The use of alternate beam shapes (Donut or Top-hat beam profiles) and its effect on cracking, residual stresses and high temperature performance is an interesting avenue of research.

All the residual stress characterizations in this thesis focused on the sub-surface residual stresses. Further understanding of how different PBF–LB processes affect the bulk residual stresses in a complex geometry, for example cruciform or turbine blades, is required.

Alternative AM technologies such as Powder Bed Fusion – Electron Beam are of high interest. This is due to the increased flexibility with scanning strategies particularly spot melting and the high pre-heating temperatures, can be beneficial to reduce cracking and tailor microstructure for improved creep performance.

Tailored HIP strategy combining residual stress relief and solution heat treatment along with the *pre-pressurisation* strategy is of interest, especially to understand macro-cracking behavior. Additionally, the possibility of creating interlocking microstructure through heat treatment is interesting to limit the easier crack propagation and improve creep performance in the horizontal direction.

All the creep tests performed in this thesis were at one condition of 871 °C (380 MPa) (Paper VII and Paper VIII). Creep tests at different loads and temperatures need to be done to have an improved understanding of the creep performance. Furthermore, understanding fatigue behavior, particularly thermo-mechanical fatigue for the different microstructures (equiaxed and columnar) obtained, is of interest.

[ - 36 - ]
------------

# Acknowledgements

Professor Eduard Hryha and Adjunct Professor Håkan Brodin, thank you both for giving me this opportunity to work on this exciting topic. I would also like to thank you both for the interesting discussions, feedback, encouragement and support.

Professor Lars Nyborg, my examiner, thank you for the support and being enthusiastic as always about research.

Professor Johan Moverare and Professor Ru Peng from Linköping University, thank you for the discussions and contributions towards my work.

Höganäs AB, Quintus AB, Siemens Energy AB and EOS Finland Oy are acknowledged for their valuable contribution and discussions in the MAGDA project (Materials for green hydrogen fueled gas turbines through additive manufacturing) funded by VINNOVA.

I would also like to acknowledge Centre for Additive Manufacture Metal (CAM<sup>2</sup>) funded by VINNOVA under which part of this thesis work has been carried out.

Adjunct Professor Sven Bengtsson from Höganäs AB, thank you for your support with powders and chemical analysis.

Johannes Gårdstam from Quintus AB, thank you for carrying out the different HIP cycles.

Dr. Jinghao Xu from Linköping University, thank you for the deep discussions, support and being a good companion to some of the conferences. I would also like to thank you for performing the mechanical tests.

Dr. A. Shaafi Shaikh from EOS Finland, thank you for the discussion and sharing your knowledge about AM and superalloys.

I would also like to acknowledge the fruitful collaboration with Bundesanstalt für Materialforschung und-prüfung (BAM) in Berlin. Special thanks go to Dr. Tatiana Mishurova (ex-BAM, now-HZB) and Dr. Jakob Schröder, for assistance with XCT and residual stress measurements. I would also like to thank Alexander Evans and Giovanni Bruno for their support and discussions.

I would also like to acknowledge Dr. Andrea Fazi, Dr. Severin Jakob and Professor Mattias Thuvander from Department of Physics at Chalmers for their support, discussion, and assistance with APT measurements. Also, thanks to research engineers Dr. Stefan Gustafsson and Dr. Katarina Logg from Chalmers Materials Analysis Laboratory (CMAL).

Dr. Bharat Mehta and Andreas Markström from Thermo-Calc Software AB are acknowledged for their support with the software and simulations.

I would also like to thank Axel Hultgren Foundation for the scholarships that supported in attending many of the conferences that sparked many interesting discussions.

Professor Uta Klement, apart from being my manager, thank you for answering all my questions regarding EBSD and for bringing cECCI capability to our microscope.

This thesis would not have been possible without support from the research engineers: Dr. Yiming Yao, Roger Sagdahl, Dr. Antonio Mulone and Johnny Hamnesjö Olausson. I would also like to acknowledge colleagues from the PMAM group, MM and EM divisions for the lively atmosphere and fika talks.

Special thanks to Drs. Anok, **Bala**, Camille, Dmitri, Gowtham, Rasmus, and to-be-Drs. Plinio, Sahith, Satya, Sofia and Vishnu.

I also would like to acknowledge my thesis and intern students: Aakash, Nikolaos, Thiemo, Camille and Chloé.

\_

Dr. Rehan Ahmed (from Heriot-Watt University), thank you for sparking my curiosity in material science. Without your influence and mentorship, I probably would not have shifted my field to material science, and I most probably would not have started a PhD.

I also would like to acknowledge Fahmi Al-Shawwa and Axel Fernandes from Immensa Technology Labs where I was introduced to the world of 3D printing. I also would like to acknowledge my co-workers from Immensa: Elias, Nissar, Hans, Azhan and Harry. I also would like to acknowledge Edem who is not with us anymore.

Dad and Mom, my deepest gratitude goes to you for your support throughout these years. Dad, thank you for sparking my curiosity in Physics, to be inquisitive and for motivating me to always give my best in everything that I do.

Absara ♥, thank you for your love, support, motivation and being my personal cheerleader throughout this journey. And little Haniya who I am excited to meet.

Ahmed Fardan Jabir Hussain Göteborg, 18<sup>th</sup> November 2025

## References

- [1] ISO/ASTM, ISO/ASTM 52911-1:2019, Additive manufacturing Design Part 1: Laser-based powder bed fusion of metals, 2019. https://www.iso.org/standard/72951.html.
- [2] W.E. Frazier, Metal additive manufacturing: A review, J. Mater. Eng. Perform. 23 (2014) 1917–1928. https://doi.org/10.1007/s11665-014-0958-z.
- [3] O. Andersson, A. Graichen, H. Brodin, V. Navrotsky, Developing Additive Manufacturing Technology for Burner Repair, J. Eng. Gas Turbines Power 139 (2017) 1–9. https://doi.org/10.1115/1.4034235.
- [4] Siemens AG, Siemens and E.ON reach milestone with 3D-printed burner for SGT-700 gas turbine, PR2018090304PSEN (2018). https://press.siemens.com/global/en/pressrelease/siemens-and-eon-reach-milestone-3d-printed-burner-sgt-700-gas-turbine.
- [5] M. Lindbäck, K. Frankolin, E. Tuneskog, B. Karlsson, L. Wang, Development and Validation Under Engine Operation Environment of Addtively Manufactured Hot Turbine Parts, 2023. https://doi.org/10.1115/GT2023-103771.
- [6] K. Harris, G.L. Erickson, R.E. Schwer, MAR-M247 derivations—CM247 LC DS alloy, CMSX single crystal alloys, properties and performance, Superalloys 1984 (1984) 221–230.
- [7] K. Harris, High ductility Nickel alloy directional casting of parts for high temperature and stress operation, US4461659A, 1981. https://patents.google.com/patent/US4461659A/en.
- [8] W. Danesi, R. Thielemann, NICKEL BASE ALLOY, US3720509A, 1970. https://doi.org/10.17077/0031-0360.24332.
- [9] C.T. Sims, N.S. Stoloff, W.C. Hagel, Superalloys II, Wiley-Interscience, New York, NY, United States, 1987. https://www.osti.gov/biblio/5452409.
- [10] B. Geddes, H. Leon, X. Huang, Superalloys Alloying and Performance, ASM International, 2010. https://app.knovel.com/hotlink/pdf/id:kt008N7R71/superalloys-alloying/introduction BT - Superalloys - Alloying and Performance.
- [11] R.C. Reed, The Superalloys fundamentals and applications, 2006. https://doi.org/10.1017/CBO9780511541285.
- [12] N. Cumpsty, Jet Propulsion: A Simple Guide to the Aerodynamics and Thermodynamic Design and Performance of Jet Engines, Cambridge University Press, 1997.
- [13] S. Tanigawa, M. Kataoka, M. Taneike, R. Ito, T. Komaki, N. Motoyama,

- Development of metal AM technology for gas turbine components, J. Glob. Power Propuls. Soc. (2023) 49–65. https://doi.org/10.33737/jgpps/163429.
- [14] E. Stefan, B. Talic, Y. Larring, A. Gruber, T.A. Peters, Materials challenges in hydrogen-fuelled gas turbines, Int. Mater. Rev. 67 (2022) 461–486. https://doi.org/10.1080/09506608.2021.1981706.
- [15] M. Alnaeli, M. Alnajideen, R. Navaratne, H. Shi, P. Czyzewski, P. Wang, S. Eckart, A. Alsaegh, A. Alnasif, S. Mashruk, A. Valera Medina, P.J. Bowen, High-Temperature Materials for Complex Components in Ammonia/Hydrogen Gas Turbines: A Critical Review, Energies 16 (2023). https://doi.org/10.3390/en16196973.
- [16] G. Blaine, L. Hugo, H. Xiao, Superalloys Alloying and Performance, ASM International, 2010.
- [17] B. Schulz, T. Leitner, S. Primig, In-situ observation of the incipient melting of borides and its effect on the hot-workability of Ni-based superalloys, J. Alloys Compd. 956 (2023) 170324. https://doi.org/10.1016/j.jallcom.2023.170324.
- [18] P. Kontis, H.A.M. Yusof, S. Pedrazzini, M. Danaie, K.L. Moore, P.A.J. Bagot, M.P. Moody, C.R.M. Grovenor, R.C. Reed, On the effect of boron on grain boundary character in a new polycrystalline superalloy, Acta Mater. 103 (2016) 688–699. https://doi.org/10.1016/j.actamat.2015.10.006.
- [19] A.S. Shaikh, E. Hryha, M. Sattari, M. Thuvander, K. Minet-Lallemand, Concurrent Improvement of Additive Manufacturing Processability and Creep Performance in a Legacy Polycrystalline Superalloy Using Grain Boundary Strengtheners, in: J. Cormier, I. Edmonds, S. Forsik, P. Kontis, C. O'Connell, T. Smith, A. Suzuki, S. Tin, J. Zhang (Eds.), Springer Nature Switzerland, Cham, 2024: pp. 883–896. https://doi.org/10.1007/978-3-031-63937-1 82.
- [20] A. Després, S. Antonov, C. Mayer, C. Tassin, M. Veron, J.J. Blandin, P. Kontis, G. Martin, On the role of boron, carbon and zirconium on hot cracking and creep resistance of an additively manufactured polycrystalline superalloy, Materialia 19 (2021). https://doi.org/10.1016/j.mtla.2021.101193.
- [21] P.D. Enrique, T. Minasyan, E. Toyserkani, Laser powder bed fusion of difficult-to-print γ' Ni-based superalloys: A review of processing approaches, properties, and remaining challenges, Addit. Manuf. 106 (2025) 104811. https://doi.org/10.1016/j.addma.2025.104811.
- [22] ISO/ASTM, ISO/ASTM 52900:2021, Additive manufacturing General principles Fundamentals and vocabulary, 2021. www.sis.se.
- [23] E. Hryha, D. Riabov, Metal Powder Production for Additive Manufacturing, in: F.G.B.T.-E. of M.M. and A. Caballero (Ed.), Elsevier, Oxford, 2022: pp. 264–271. https://doi.org/10.1016/B978-0-12-819726-4.00089-2.

- [24] R. Gunnerek, Z. Chen, E. Hryha, Impact of high-productivity process parameters in powder bed fusion—laser beam on microstructure of stainless steel 316L, Eur. J. Mater. 3 (2023). https://doi.org/10.1080/26889277.2023.2292987.
- [25] R. Gunnerek, T. Mishurova, G. Bruno, E. Hryha, Correlation between High Build Speed Process Parameters and Pore Characteristics of 316L Stainless Steel Manufactured by Powder Bed Fusion Laser Beam, Funtai Oyobi Fummatsu Yakin/Journal Japan Soc. Powder Powder Metall. 72 (2025) S475–S481. https://doi.org/10.2497/jjspm.15B-T6-21.
- [26] M.C. Lam, S.C.V. Lim, H. Song, Y. Zhu, X. Wu, A. Huang, Scanning strategy induced cracking and anisotropic weakening in grain texture of additively manufactured superalloys, Addit. Manuf. 52 (2022) 102660. https://doi.org/10.1016/j.addma.2022.102660.
- [27] A. Leicht, C.H. Yu, V. Luzin, U. Klement, E. Hryha, Effect of scan rotation on the microstructure development and mechanical properties of 316L parts produced by laser powder bed fusion, Mater. Charact. 163 (2020) 2–10. https://doi.org/10.1016/j.matchar.2020.110309.
- [28] A. Soltani-Tehrani, M.S. Yasin, S. Shao, N. Shamsaei, Effects of Stripe Width on the Porosity and Mechanical Performance of Additively Manufactured Ti-6Al-4V Parts, Proc. 32nd Solid Free. Fabr. Symp. (2021) 1061–1075.
- [29] X. Zhang, R. Li, Y. Ma, H. Wu, G. Fan, Effects of Hot Isostatic Pressing on the Microstructure and Mechanical Properties of K418 Alloys Fabricated by Selective Laser Melting, Jom 76 (2024) 6240–6251. https://doi.org/10.1007/s11837-024-06765-2.
- [30] M. Ahlfors, Hot Isostatic Pressing for Metal Additive Manufacturing, in: ASM Handb. Addit. Manuf. Process., 2020: pp. 316–323. https://doi.org/10.31399/asm.hb.v24.a0006552.
- [31] W. Hearn, P. Harlin, E. Hryha, Development of powder bed fusion—laser beam process for AISI 4140, 4340 and 8620 low-alloy steel, Powder Metall. 66 (2023) 94–106. https://doi.org/10.1080/00325899.2022.2134083.
- [32] A.S. Shaikh, F. Schulz, K. Minet-Lallemand, E. Hryha, Microstructure and mechanical properties of Haynes 282 superalloy produced by laser powder bed fusion, Mater. Today Commun. 26 (2021) 102038. https://doi.org/10.1016/j.mtcomm.2021.102038.
- [33] L.N. Carter, C. Martin, P.J. Withers, M.M. Attallah, The influence of the laser scan strategy on grain structure and cracking behaviour in SLM powder-bed fabricated nickel superalloy, J. Alloys Compd. 615 (2014) 338–347. https://doi.org/10.1016/j.jallcom.2014.06.172.
- [34] A.S. Shaikh, Development of a γ' Precipitation Hardening Ni-Base Superalloy

- for Additive Manufacturing, Chalmers University of Technology, 2018. https://hdl.handle.net/20.500.12380/255645.
- [35] D.L. Wenzler, K. Bergmeier, S. Baehr, J. Diller, M.F. Zaeh, A Novel Methodology for the Thermographic Cooling Rate Measurement during Powder Bed Fusion of Metals Using a Laser Beam, Integr. Mater. Manuf. Innov. 12 (2023) 41–51. https://doi.org/10.1007/s40192-023-00291-w.
- [36] T. Furumoto, K. Oishi, S. Abe, K. Tsubouchi, M. Yamaguchi, A.T. Clare, Evaluating the thermal characteristics of laser powder bed fusion, J. Mater. Process. Technol. 299 (2022). https://doi.org/10.1016/j.jmatprotec.2021.117384.
- [37] J. Xu, P. Kontis, R.L. Peng, J. Moverare, Modelling of additive manufacturability of nickel-based superalloys for laser powder bed fusion, Acta Mater. 240 (2022) 118307. https://doi.org/10.1016/j.actamat.2022.118307.
- [38] S. Griffiths, H. Ghasemi Tabasi, T. Ivas, X. Maeder, A. De Luca, K. Zweiacker, R. Wróbel, J. Jhabvala, R.E. Logé, C. Leinenbach, Combining alloy and process modification for micro-crack mitigation in an additively manufactured Ni-base superalloy, Addit. Manuf. 36 (2020). https://doi.org/10.1016/j.addma.2020.101443.
- [39] J. Xu, H. Gruber, R.L. Peng, J. Moverare, A novel γ'-strengthened nickel-based superalloy for laser powder bed fusion, Materials (Basel). 13 (2020) 1–12. https://doi.org/10.3390/ma13214930.
- [40] A. Fardan, A. Fazi, R.L. Peng, T. Mishurova, M. Thuvander, G. Bruno, H. Brodin, E. Hryha, Fine-Tuning Melt Pools and Microstructures: Taming Cracks in Powder Bed Fusion Laser Beam of a non-weldable Ni-base Superalloy, Materialia (2024) 102059. https://doi.org/10.1016/j.mtla.2024.102059.
- [41] A.S. Shaikh, M. Rashidi, K. Minet-Lallemand, E. Hryha, On as-built microstructure and necessity of solution treatment in additively manufactured Inconel 939, Powder Metall. 66 (2023) 3–11. https://doi.org/10.1080/00325899.2022.2041787.
- [42] O. Adegoke, C. Kumara, M. Thuvander, F. Deirmina, J. Andersson, H. Brodin, P. Harlin, R. Pederson, Scanning electron microscopy and atom probe tomography characterization of laser powder bed fusion precipitation strengthening nickel-based superalloy, Micron 171 (2023) 103472. https://doi.org/10.1016/j.micron.2023.103472.
- [43] A. Després, S. Antonov, C. Mayer, M. Veron, E.F. Rauch, C. Tassin, J.-J. Blandin, P. Kontis, G. Martin, Revealing the true partitioning character of zirconium in additively manufactured polycrystalline superalloys, Addit. Manuf. Lett. 1 (2021) 100011. https://doi.org/10.1016/j.addlet.2021.100011.

- [44] J.R. Miller, J.F.S. Markanday, S.M. Fairclough, G.J. Wise, C.M.F. Rae, L.R. Owen, D. Stapleton, N. D'Souza, P.A.J. Bagot, H.J. Stone, Gamma prime precipitation in as-deposited Ni-based superalloy IN713LC, Scr. Mater. 239 (2024) 115775. https://doi.org/10.1016/j.scriptamat.2023.115775.
- [45] J.F.S. Markanday, N. D'Souza, N.L. Church, J.R. Miller, J.J.C. Pitchforth, L.D. Connor, S. Michalik, B. Roebuck, N.G. Jones, K.A. Christofidou, H.J. Stone, The Relationship Between Strain-Age Cracking and the Evolution of γ' in Laser Powder-Bed-Fusion Processed Ni-Based Superalloys, in: J. Cormier, I. Edmonds, S. Forsik, P. Kontis, C. O'Connell, T. Smith, A. Suzuki, S. Tin, J. Zhang (Eds.), Superalloys 2024, Springer Nature Switzerland, Cham, 2024: pp. 822–835.
- [46] J.F.S. Markanday, K.A. Christofidou, J.R. Miller, E.R. Livera, N.G. Jones, E.J. Pickering, W. Li, Y. Pardhi, C.N. Jones, H.J. Stone, The Microstructural Evolution of CM247LC Manufactured Through Laser Powder Bed Fusion, Metall. Mater. Trans. A Phys. Metall. Mater. Sci. (2023). https://doi.org/10.1007/s11661-022-06939-0.
- [47] P.J. Withers, K.D. Bhadeshia, Residual stress. Part 1 Measurement techniques, Mater. Sci. Technol. 17 (2001) 355–365. https://doi.org/10.1179/026708301101509980.
- [48] P.J. Withers, H.K.D.H. Bhadeshia, Residual stress. Part 2 Nature and origins, Mater. Sci. Technol. 17 (2001) 366–375. https://doi.org/https://doi.org/10.1179/026708301101510087.
- [49] M.E. Fitzpatrick, A. Lodini, Analysis of Residual Stress by Diffraction using Neutron and Synchrotron Radiation, 2003. https://doi.org/10.1201/9780203608999.
- [50] D. Jiang, Y. Tian, Y. Zhu, S. Huang, A. Huang, On the microstructure and tensile property of core-shell structured nickel-based superalloy part produced by laser powder bed fusion and hot isostatic pressing, Mater. Sci. Eng. A 870 (2023) 144833. https://doi.org/10.1016/j.msea.2023.144833.
- [51] E. Bassini, A. Sivo, P.A. Martelli, E. Rajczak, G. Marchese, F. Calignano, S. Biamino, D. Ugues, Effects of the solution and first aging treatment applied to as-built and post-HIP CM247 produced via laser powder bed fusion (LPBF), J. Alloys Compd. 905 (2022) 164213. https://doi.org/10.1016/j.jallcom.2022.164213.
- [52] A.S. Shaikh, E. Eriksson, M.H. Colliander, K. Minet-Lallemand, E. Hryha, Tailored heat treatments to enhance performance in additive manufactured HAYNES® 282® superalloy, Materialia 39 (2025). https://doi.org/10.1016/j.mtla.2025.102334.
- [53] M.S. Kenevisi, P.A. Martelli, I. Titonel, E. Bassini, G. Marchese, D. Ugues,

- The effect of solution annealing on additively manufactured and hot isostatically pressed René 80 Ni-based superalloy, J. Mater. Res. Technol. 33 (2024) 6591–6600. https://doi.org/10.1016/j.jmrt.2024.11.003.
- [54] P.A. Martelli, E. Bassini, D. Ugues, The effect of hot isostatic pressing pressure level and solution annealing cooling rate on CM247 LC nickel-based superalloy processed by laser-based powder bed fusion, Prog. Addit. Manuf. (2024). https://doi.org/10.1007/s40964-024-00645-6.
- [55] L. Liu, D. Wang, G. Deng, C. Han, H. Zhou, C. Tan, Y. Long, Z. Liu, M. Zhang, C. Yang, Y. Yang, Crack inhibition and mechanical property enhancement of a CM247LC alloy fabricated by laser powder bed fusion through remelting strategy, Mater. Charact. 214 (2024) 114073. https://doi.org/10.1016/j.matchar.2024.114073.
- [56] Y. Wang, W. Guo, H. Zheng, Y. Xie, X. Zhang, H. Li, M. Xu, H. Zhang, Microstructure, crack formation and improvement on Nickel-based superalloy fabricated by powder bed fusion, J. Alloys Compd. 962 (2023) 171151. https://doi.org/10.1016/j.jallcom.2023.171151.
- [57] B. Kumar, S. Sahu, D. Srinivasan, N.J. Balila, Influence of Heat Input on Solidification Cracking in Additively Manufactured CM247LC Ni-based Superalloy, Metall. Mater. Trans. A (2022). https://doi.org/10.1007/s11661-023-07027-7.
- [58] Y.T. Tang, C. Panwisawas, J.N. Ghoussoub, Y. Gong, J.W.G. Clark, A.A.N. Németh, D.G. McCartney, R.C. Reed, Alloys-by-design: Application to new superalloys for additive manufacturing, Acta Mater. 202 (2021) 417–436. https://doi.org/10.1016/j.actamat.2020.09.023.
- [59] M.A.L. Phan, O. Dew, I. Todd, Predictive process diagram for parameters selection in laser powder bed fusion to achieve high-density and low-cracking built parts, Addit. Manuf. 85 (2024) 104145. https://doi.org/10.1016/j.addma.2024.104145.
- [60] K. Heck, J.R. Blackford, R.F. Singer, Castability of directionally solidified nickel base superalloys, Mater. Sci. Technol. 15 (1999) 213–220. https://doi.org/10.1179/026708399101505617.
- [61] S. Kou, Welding metallurgy, 2. ed., Wiley, 2003.
- [62] J.N. Ghoussoub, Y.T. Tang, W.J.B. Dick-Cleland, A.A.N. Németh, Y. Gong, D.G. McCartney, A.C.F. Cocks, R.C. Reed, On the Influence of Alloy Composition on the Additive Manufacturability of Ni-Based Superalloys, Metall. Mater. Trans. A 53 (2022) 962–983. https://doi.org/10.1007/s11661-021-06568-z.
- [63] M. Cloots, P.J. Uggowitzer, K. Wegener, Investigations on the microstructure and crack formation of IN738LC samples processed by selective laser melting

- using Gaussian and doughnut profiles, Mater. Des. 89 (2016) 770–784. https://doi.org/10.1016/j.matdes.2015.10.027.
- [64] H. Gruber, E. Hryha, K. Lindgren, Y. Cao, M. Rashidi, L. Nyborg, The Effect of Boron and Zirconium on the Microcracking Susceptibility of IN-738LC Derivatives in Laser Powder Bed Fusion, Appl. Surf. Sci. 573 (2021) 151541. https://doi.org/10.1016/j.apsusc.2021.151541.
- [65] Z. Sun, Y. Ma, D. Ponge, S. Zaefferer, E.A. Jägle, B. Gault, A.D. Rollett, D. Raabe, Thermodynamics-guided alloy and process design for additive manufacturing, Nat. Commun. 13 (2022) 1–12. https://doi.org/10.1038/s41467-022-31969-y.
- [66] A. Hariharan, L. Lu, J. Risse, A. Kostka, B. Gault, E.A. Jägle, D. Raabe, Misorientation-dependent solute enrichment at interfaces and its contribution to defect formation mechanisms during laser additive manufacturing of superalloys, Phys. Rev. Mater. 3 (2019) 123602. https://doi.org/10.1103/PhysRevMaterials.3.123602.
- [67] E.B. Raeker, K.M. Pusch, N. Zhou, A.J. Forsik, D. Austin, M.M. Kirka, T.M. Pollock, Minor elements and solidification cracking during laser powder-bed fusion of a high γ ′ CoNi-base superalloy, Metall. Mater. Trans. A (2022). https://doi.org/10.1007/s11661-023-06957-6.
- [68] A.S. Shaikh, Additive manufacturing of Ni-base superalloys: Processing, heat treatment, productivity, and properties, Chalmers University of Technology, 2025. https://research.chalmers.se/en/publication/546050.
- [69] L. Ma, D. Wang, G. Zhang, J. Shen, J. Zhang, Effect of Hf on microstructure and creep properties of nickel-based bicrystal superalloy with different grain boundaries misorientations, Mater. Sci. Eng. A 935 (2025). https://doi.org/10.1016/j.msea.2025.148371.
- [70] B. Wei, Z. Liu, B. Cao, B. Nong, Y. Zhang, Y. Ren, H. Zhou, S. Wei, Cracking inhibition of nano-TiC reinforced René 104 superalloy fabricated by selective laser melting, J. Alloys Compd. 881 (2021) 160413. https://doi.org/10.1016/j.jallcom.2021.160413.
- [71] C. Guo, Z. Yu, X. Hu, G. Li, F. Zhou, Z. Xu, S. Han, Y. Zhou, R.M. Ward, Q. Zhu, Y2O3 nanoparticles decorated IN738LC superalloy manufactured by laser powder bed fusion: Cracking inhibition, microstructures and mechanical properties, Compos. Part B Eng. 230 (2022) 109555. https://doi.org/10.1016/j.compositesb.2021.109555.
- [72] L.N. Carter, M.M. Attallah, R.C. Reed, Laser powder bed fabrication of nickel-base superalloys: Influence of parameters; characterisation, quantification and mitigation of cracking, Proc. Int. Symp. Superalloys (2012) 577–586. https://doi.org/10.7449/2012/superalloys 2012 577 586.

- [73] D. Grange, J.D. Bartout, B. Macquaire, C. Colin, Processing a non-weldable nickel-base superalloy by Selective Laser Melting: role of the shape and size of the melt pools on solidification cracking, Materialia 12 (2020). https://doi.org/10.1016/j.mtla.2020.100686.
- [74] A. De Luca, C. Kenel, S. Griffiths, S.S. Joglekar, C. Leinenbach, D.C. Dunand, Microstructure and defects in a Ni-Cr-Al-Ti γ/γ' model superalloy processed by laser powder bed fusion, Mater. Des. 201 (2021). https://doi.org/10.1016/j.matdes.2021.109531.
- [75] J.H. Boswell, D. Clark, W. Li, M.M. Attallah, Cracking during thermal post-processing of laser powder bed fabricated CM247LC Ni-superalloy, Mater. Des. 174 (2019) 107793. https://doi.org/10.1016/j.matdes.2019.107793.
- [76] J.N. DuPont, J.C. Lippold, S.D. Kiser, Welding Metallurgy and Weldability of Nickel-Base Alloys, Wiley Online Library, 2009. https://doi.org/10.1002/9780470500262.
- [77] X. Wang, L.N. Carter, B. Pang, M.M. Attallah, M.H. Loretto, Microstructure and yield strength of SLM-fabricated CM247LC Ni-Superalloy, Acta Mater. 128 (2017) 87–95. https://doi.org/10.1016/j.actamat.2017.02.007.
- [78] F. Schulz, K. Lindgren, J. Xu, E. Hryha, Gamma prime formation in nickel-based superalloy IN738LC manufactured by laser powder bed fusion, Mater. Today Commun. 38 (2024) 107905. https://doi.org/10.1016/j.mtcomm.2023.107905.
- [79] P.D. Enrique, T. Minasyan, E. Toyserkani, Laser powder bed fusion of difficult-to-print γ' Ni-based superalloys: A review of processing approaches, properties, and remaining challenges, Addit. Manuf. 106 (2025). https://doi.org/10.1016/j.addma.2025.104811.
- [80] V. Kalyanasundaram, A. De Luca, R. Wróbel, J. Tang, S.R. Holdsworth, C. Leinenbach, E. Hosseini, Tensile and creep-rupture response of additively manufactured nickel-based superalloy CM247LC, Addit. Manuf. Lett. 5 (2023) 100119. https://doi.org/10.1016/j.addlet.2022.100119.
- [81] M.N. Doğu, S. Ozer, M.A. Yalçın, K. Davut, G.M. Bilgin, M.A. Obeidi, H. Brodin, H. Gu, D. Brabazon, Effect of solution heat treatment on the microstructure and crystallographic texture of IN939 fabricated by powder bed fusion-laser beam, J. Mater. Res. Technol. 24 (2023) 8909–8923. https://doi.org/10.1016/j.jmrt.2023.05.152.
- [82] S. Banoth, C.W. Li, Y. Hiratsuka, K. Kakehi, The effect of recrystallization on creep properties of alloy in 939 fabricated by selective laser melting process, Metals (Basel). 10 (2020) 1–16. https://doi.org/10.3390/met10081016.
- [83] R. Engeli, Selective Laser Melting & Engelia Treatment of γ´ Strengthened Ni-base Superalloys for High Temperature Applications, ETH Zurich, 2017.

- https://doi.org/10.3929/ethz-b-000000074.
- [84] H.E. Huang, C.H. Koo, Characteristics and Mechanical Properties of Polycrystalline CM 247 LC Superalloy Casting, Mater. Trans. 45 (2004) 562– 568. https://doi.org/10.2320/matertrans.45.562.
- [85] S. Megahed, K.M. Krämer, C. Heinze, C. Kontermann, A. Udoh, S. Weihe, M. Oechsner, Creep of IN738LC manufactured with laser powder bed fusion: effect of build orientation and twinning, Mater. High Temp. 41 (2024) 95–105. https://doi.org/10.1080/09603409.2023.2261665.
- [86] S. Megahed, K.M. Krämer, C. Heinze, C. Kontermann, A. Udoh, S. Weihe, M. Oechsner, Influence of build orientation on the creep behavior of IN738LC manufactured with laser powder bed fusion, Mater. Sci. Eng. A 878 (2023). https://doi.org/10.1016/j.msea.2023.145197.
- [87] S. Hocine, H. Van Swygenhoven, S. Van Petegem, C.S.T. Chang, T. Maimaitiyili, G. Tinti, D. Ferreira Sanchez, D. Grolimund, N. Casati, Operando X-ray diffraction during laser 3D printing, Mater. Today 34 (2020) 30–40. https://doi.org/10.1016/j.mattod.2019.10.001.
- [88] S. Hocine, S. Van Petegem, U. Frommherz, G. Tinti, N. Casati, D. Grolimund, H. Van Swygenhoven, A miniaturized selective laser melting device for operando X-ray diffraction studies, Addit. Manuf. 34 (2020) 101194. https://doi.org/10.1016/j.addma.2020.101194.
- [89] F. Bachmann, R. Hielscher, H. Schaeben, Texture Analysis with MTEX–Free and Open Source Software Toolbox, Solid State Phenom. 160 (2010) 294–306. https://doi.org/10.4028/www.scientific.net/SSP.160.63.
- [90] S. Zaefferer, N.N. Elhami, Theory and application of electron channelling contrast imaging under controlled diffraction conditions, Acta Mater. 75 (2014) 20–50. https://doi.org/10.1016/j.actamat.2014.04.018.
- [91] S. Zaefferer, New developments of computer-aided crystallographic analysis in transmission electron microscopy, J. Appl. Crystallogr. 33 (2000) 10–25. https://doi.org/10.1107/S0021889899010894.
- [92] W. Lefebvre, F. Vurpillot, X. Sauvage, Atom Probe Tomography: Put Theory Into Practice, Academic Press, London, 2016.
- [93] K. Thompson, D. Lawrence, D.J. Larson, J.D. Olson, T.F. Kelly, B. Gorman, In situ site-specific specimen preparation for atom probe tomography, Ultramicroscopy 107 (2007) 131–139. https://doi.org/10.1016/j.ultramic.2006.06.008.
- [94] V. Hauk, Structural and Residual Stress Analysis by Nondestructive Methods, Elsevier Science, 1997. https://doi.org/10.1016/B978-0-444-82476-9.X5000-2.
- [95] H. Andersson-Östling, R. Sandström, Survey of creep properties of copper

- intended for nuclear waste disposal, Stockholm, 2009. https://www.skb.com/publication/2029174/TR-09-32.pdf.
- [96] D.M. Collins, N. D'Souza, C. Panwisawas, C. Papadaki, G.D. West, A. Kostka, P. Kontis, Spinodal decomposition versus classical γ' nucleation in a nickel-base superalloy powder: An in-situ neutron diffraction and atomic-scale analysis, Acta Mater. 200 (2020) 959–970. https://doi.org/10.1016/j.actamat.2020.09.055.
- [97] I. Serrano-Munoz, T. Mishurova, T. Thiede, M. Sprengel, A. Kromm, N. Nadammal, G. Nolze, R. Saliwan-Neumann, A. Evans, G. Bruno, The residual stress in as-built Laser Powder Bed Fusion IN718 alloy as a consequence of the scanning strategy induced microstructure, Sci. Rep. 10 (2020) 1–15. https://doi.org/10.1038/s41598-020-71112-9.